The Astrophysical Journal, 710:1032–1062, 2010 February 20 doi:10.1088/0004-637X/710/2/1032

NEW LIMITS ON AN INTERMEDIATE-MASS BLACK HOLE IN OMEGA CENTAURI. I. *HUBBLE SPACE TELESCOPE* PHOTOMETRY AND PROPER MOTIONS*

Jay Anderson and Roeland P. van der Marel
Space Telescope Science Institute, Baltimore, MD 21218, USA; jayander@stsci.edu, marel@stsci.edu
Received 2009 May 4; accepted 2009 December 21; published 2010 January 27

ABSTRACT

We analyze data from the *Hubble Space Telescope*'s (*HST*) Advanced Camera for Surveys of the globular cluster (GC) Omega Cen. We construct a photometric catalog of 1.2×10^6 stars over a $10' \times 10'$ central field down to below $B_{\rm F435W} = 25$ ($M \sim 0.35\,M_\odot$). The 2.5 to 4 year baseline between observations yields a catalog of some 10^5 proper motions over a smaller area, with 53,382 "high-quality" measurements in a central $R \lesssim 2'$ field. Artificial-star tests characterize the photometric incompleteness. We determine the cluster center to $\sim 1''$ accuracy from star counts using two different methods, one based on isodensity contours and the other on "pie slices." We independently confirm the result by determining also the kinematical center of the *HST* proper motions, as well as the center of unresolved light seen in Two Micron All Sky Survey data. All results agree to within their $1''$–$2''$ levels of uncertainty. The proper-motion dispersion of the cluster increases gradually inward, but there is no variation in kinematics with position within the central $\sim 15''$: there is no dispersion cusp and no stars with unusually high velocities. We measure for the first time in any GC the variation in internal kinematics along the main sequence. The variation of proper-motion dispersion with mass shows that the cluster is not yet in equipartition. There are no differences in proper-motion kinematics between the different stellar populations of Omega Cen. Our results do not confirm the arguments put forward by Noyola, Gebhardt, and Bergmann to suspect an intermediate-mass black hole (IMBH) in Omega Cen. They determined line-of-sight velocity dispersions in two $5'' \times 5''$ fields, and reported higher motions in their central field. We find the proper-motion kinematics to be the same in both fields. Also, we find that they (as well as other previous studies) did not accurately identify the cluster center, so that both of their fields are in fact $12''$ from the true center. We also do not confirm the central density cusp they reported (in part due to the different center, and in part due to biases induced by their use of unresolved light). The surface number-density distribution near the center does not differ strongly from a single-mass King model, although a shallow cusp may not be ruled out. In the companion paper, which is Paper II in this series, we present new dynamical models for the high-quality data presented here, with the aim of putting quantitative constraints on the mass of any possible IMBH.

Key words: catalogs – globular clusters: general – globular clusters: individual (Omega Cen) – stars: kinematics and dynamics – techniques: image processing – techniques: photometric

Online-only material: color figures, machine-readable tables, tar file of FITS images

1. INTRODUCTION

There is much current interest in finding black holes at the centers of globular clusters (GCs). Supermassive ($\gtrsim 10^6\,M_\odot$) black holes are known to exist at the centers of galaxies, and it has been demonstrated that the black hole mass is correlated with the velocity dispersion of the galaxy. If GCs house massive central black holes that follow the same correlation, then based on their central velocity dispersions of order ~ 10 km s^{-1}, we would expect to find an intermediate-mass black hole (IMBH) with a mass of a few thousand solar masses (Gebhardt et al. 2002). Plausible formation scenarios exist to form such IMBHs in the centers of GCs from realistic initial conditions (Portegies Zwart & McMillan 2002). Determining whether GCs harbor IMBHs will answer important questions about how clusters form, and about what kinds of circumstances give rise to IMBHs (e.g., van der Marel 2004).

An IMBH should induce a power-law cusp in the stellar-density profile (Baumgardt et al. 2005). Such cusps are not uncommon in GCs (Noyola & Gebhardt 2006). However, various stages of core collapse can introduce similar cusps, so observing a cusp is not definitive evidence for an IMBH. X-ray or radio emission may point toward accretion onto an IMBH (Pooley & Rappaport 2006; Kong 2007; Ulvestad et al. 2007), but other explanations for the emission are difficult to rule out. Moreover, GCs generally have little gas to accrete. The most unambiguous way to identify and weigh an IMBH is therefore to find the signature it induces in the kinematics of nearby stars. There are two ways in which kinematics could identify an IMBH. First, there may be a general increase in the velocity dispersion toward the center that cannot be accounted for by the visible matter. Second, there may be stars moving faster than would be allowed by the cluster's nominal escape velocity (Drukier & Bailyn 2003). One might even hope to observe stars in Keplerian orbit, as has been seen at the center of our own Galaxy (Genzel et al. 2003; Ghez et al. 2005).

Kinematical evidence for IMBHs on the basis of an increase in the line-of-sight velocity dispersion toward the center has been presented for the GCs M15 and G1 (van der Marel et al. 2002; Gerssen et al. 2002; Gebhardt et al. 2002, 2005). However, in M15 the implied dark mass could also be attributed to segregation of dark remnants towards the center (e.g., Baumgardt et al. 2003a), while in G1 the statistical significance of the implied dark mass is not strong (Baumgardt et al. 2003b). The limitations of these past investigations are due in part to their use of line-of-sight velocities. Proper motions can generally put

* Based on observations with the NASA/ESA *Hubble Space Telescope*, obtained at the Space Telescope Science Institute, which is operated by AURA, Inc., under NASA contract NAS 5-26555.

more powerful constraints on an IMBH than can line-of-sight velocities, because they can be measured for many more stars. Since proper motions probe two components of the motion, they also yield better constraints on the velocity anisotropy and therefore help break the well-known degeneracy between mass and anisotropy. In cases where one can assume spherical symmetry, this degeneracy is resolved completely (Leonard & Merritt 1989). Furthermore, while spectroscopic line-of-sight velocity studies are limited to the bright stars, the *Hubble Space Telescope* (*HST*) can observe proper motions for the much more plentiful main-sequence (MS) stars. This gives better statistics to probe closer to the center. IMBH limits from *HST* proper motions have been presented for M15 (McNamara et al. 2003; van den Bosch et al. 2006) and 47 Tuc (McLaughlin et al. 2006). These studies relied, at least in part, on data from the Wide Field and Planetary Camera 2 (WFPC2) instrument. Several studies have since been started or planned to study this problem exclusively with data from newer Advanced Camera for Surveys (ACS) or Wide Field Camera 3 (WFC3) instruments for larger samples of clusters (e.g., GO-9835 and GO-10474, PI: Drukier; GO-10401/10841, PI: Chandar; GTO-10335/11801, PI: Ford; and GO-11609, PI: Chaname). Two epochs are already in-hand for several of the target clusters in these samples and results may start to come out soon.

Recently, Noyola et al. (2008, NGB08) presented a new study of the GC Omega Cen. They used Gemini integral-field unit (IFU) spectroscopy to measure the line-of-sight velocity dispersion of unresolved light in two $5'' \times 5''$ fields, one at the cluster center and one at $R = 14''$ from the center. The dispersion in the central field (23.0 ± 2.0 km s^{-1}) exceeded that in the off-center field (18.6 ± 1.6 km s^{-1}). Based on this increase toward the center they argued for the presence of an IMBH of mass $4.0^{+0.75}_{-1.0} \times 10^4\ M_\odot$. NGB08 also measured the surface-brightness profile of unresolved light from *HST*/ACS images. They found it to have a shallow central cusp of logarithmic slope $\gamma = 0.08 \pm 0.03$, also consistent with the presence of an IMBH.

A considerable amount of ACS data of Omega Cen already exists in the *HST* Data Archive. In the present paper, we collect and analyze these data to obtain photometric and proper-motion catalogs for very large numbers of stars (of order 10^6 photometric measurements and 10^5 proper motions, respectively). We use these catalogs to perform detailed star-count and kinematical analyses. The present paper is confined to the observational domain as much as possible, and we focus on testing and augmenting the results of NGB08. Detailed dynamical modeling of the new data is presented in a companion paper (van der Marel & Anderson 2010, Paper II).

This paper is organized as follows. In Section 2, we give an overview of the three ACS/WFC data sets that are part of our study. In Section 3, we construct a photometric catalog covering the inner part of the cluster, and we determine proper motions for the stars that could be measured well in two epochs. In Section 4, we determine the position of the cluster center using our new star lists and proper motions, as well as ground-based Two Micron All Sky Survey (2MASS) data. In Section 5, we derive the number-density profile. In Section 6, we do an initial analysis of the proper-motion kinematics (with more detailed analysis following in Paper II), and we calculate the proper-motion dispersions in the fields observed by NGB08. Our results for the cluster center, density profile, and kinematical gradient are all different from those presented by NGB08. We do not confirm the arguments put forward by them to suspect an IMBH in Omega Cen. In Section 7, we combine our proper motions and photometry to determine whether the cluster core is in equipartition and to determine whether the different stellar populations in the cluster have different kinematics. Finally, in Section 8 we present the conclusions of our study.

Table 1
Data Available for the Proper-motion Study

Data Set	Central Field	Outer Field
GO-9442	3 × 340 s F435W	3 × 340 s F435W
(2002.49)	3 × 340 s F625W	3 × 340 s F625W
	4 × 440 s F658N	4 × 440 s F658N
	(Pointing 5)	(Pointings 1 and 4)
GO-10252	···	5 × 340 s F606W
(2004.95)	···	5 × 340 s F658N
GO-10755	4 × 80 s F606W	···
(2006.56)	4 × 90 s F814W	···

2. OBSERVATIONS

This paper draws on three *HST* data sets, listed in Table 1. All three were taken with the Wide-Field Channel (WFC) of the ACS, which is made up of two 2048 × 4096 pixel detectors with a pixel scale of about 50 mas pixel^{-1}, covering a rhombus-shaped field that is roughly 3.′4 on a side.

The first data set is GO-9442 (PI: Cool). It was taken over the period between 2002 June 27 and 30 and consists of a 3 × 3 mosaic of pointings, centered on the cluster center. Each pointing has three deep exposures and one shallow exposure in each of F435W ($B_{\rm F435W}$) and F625W ($R_{\rm F625W}$) and four deep observations through F658N (Hα, $H_{\rm F658N}$). Each of the deep observations was offset relative to the others, so that no star would fall in the 50-pixel-tall inter-chip gap in more than one deep exposure for each filter. The mosaic of pointings covers the inner $10' \times 10'$, extending out to about two core radii ($r_c \sim 2.'5$). The left panel of Figure 1 shows the field coverage for the $B_{\rm F435W}$ filter. *HST* mispointed in the last pointing (upper right), and there is a small gap in the field coverage there. We were careful to include the effect of this gap in our star-count analysis.

The second data set is GO-10252 (PI: Anderson). This program was taken on 2004 December 11, and consists of five deep exposures and one shallow exposure in each of F606W ($V_{\rm F606W}$) and F814W ($I_{\rm F814W}$). The goal of these observations was to construct accurate point-spread function (PSF) models and an accurate distortion solution for the two most commonly used filters, thus the various exposures have large offsets of about 500 pixels between them. Unfortunately, at the time these observations were taken, the camera was considerably out of focus (it was adjusted soon afterward), and the images were therefore not useful for their original aim of probing the "typical" PSF behavior and distortion solution. However, they are still useful for our purposes here, since we can tailor-make PSFs for these images, and can measure our motions locally, so that small errors in the global distortion solution will not impact our results. The middle panel of Figure 1 shows that this field is centered near the southeast (SE) corner of the mosaic, along the cluster's major axis. The baseline between this and the first data set is 2.49 yr.

The third data set is GO-10775 (PI: Sarajedini). These observations were taken as a part of a large survey of 65 GCs, and consist of four deep exposures and one shallow exposure in each of F606W and F814W. The observations were taken on 2006 June 22, so the baseline between this set and the first is

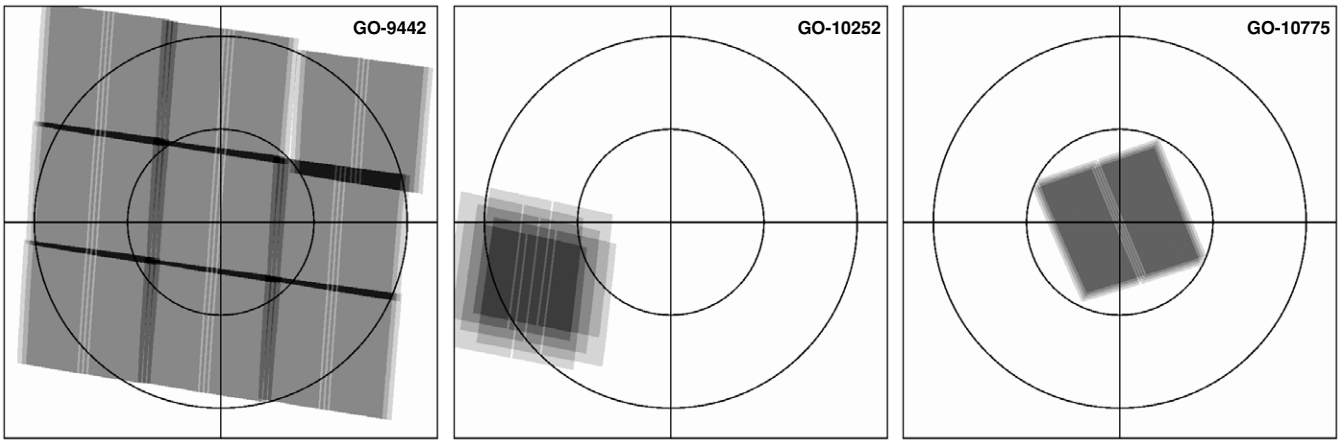

Figure 1. At each point in the field centered on Omega Cen, we show the number of exposures available for each of the two broadband colors for the three data sets. The circles indicate one core radius (2.′5) and two core radii. See the text for a description of the data in each program. The baseline between the first and second panel is 2.46 yr, and between the first and third is 4.07 yr.

4.07 years. The right panel of Figure 1 shows that this field is centered on the cluster, and on the GO-9442 mosaic.

In the following section, we describe how we constructed an extensive catalog based on the $B_{\rm F435W}$ and $R_{\rm F625W}$ exposures of the $10' \times 10'$ GO-9442 data set; then we cross-identify the same stars in the other data sets and measure proper motions.

3. REDUCTIONS

In this section, we describe how we constructed a reference frame and a catalog of photometry and proper motions. In the subsequent sections, we will then use this catalog to determine the cluster center and study the surface-density and velocity-dispersion profiles.

3.1. Reference Frame

The first task in the analysis is to construct a reference frame. We began by measuring all the bright, isolated, unsaturated stars in all the deep exposures of GO-9442. There are 36 exposures total in Hα, and 27 in each of $B_{\rm F435W}$ and $R_{\rm F425W}$. To do this, we used the publicly available software program `img2xym_WFC.09x10` (Anderson & King 2006), which employs an empirically constructed, spatially variable library PSF to determine a position and a flux for each star in each exposure. The positions are corrected for distortion using the corrections in Anderson (2005).

We began by analyzing the nine major pointings independently. For each, we took the central $R_{\rm F625W}$ observation as the basis for the reference frame of that pointing, linearly transformed the star positions from all the other images of that pointing into that frame, and determined an average position for each star that was found in at least three exposures.

The next step was to stitch together the nine overlapping frames. There was only minimal overlap between the frames. We did not want to allow for linear terms in the frame-to-frame transformation, since small errors in such terms could lead to large errors in the extrapolated field, so we stitched the pointings together by solving only for offsets and rotations, assuming the frames to have the same scales and off-axis linear terms. We first added the directly adjacent side fields to the central frame, then added the corner fields to this plus-shaped intermediate frame.

To improve this reference frame, we found a linear transformation from each exposure into the new frame, based on the positions of common stars. For each star in the reference frame, we thus had between seven and 40 estimates for its position (depending on how many images overlapped at that point), and we averaged these positions together to improve the reference frame. After a few such iterations, we found the remaining stitching errors to be less than 0.01 pixel.

The above reference frame was constructed in a distortion-corrected frame based on the central pointing. To align our frame with R.A. and decl., we found the linear transformation from this frame into the frame constructed in Anderson et al. (2008, hereafter A08), based on the GO-10775 Treasury data, which has a pixel scale of 50 mas pixel^{-1} and was aligned with R.A. and decl., and has the Harris (1996) cluster center at [3000,3000]. (We will refer to this as the "traditional" center, since it is based on the literature at the time.) We conformally transformed our reference frame into this frame and added 4000 to each coordinate, so that our entire field would be contained within the range [1:14000,1:14000], with the center close to [7000,7000]. We refer to this frame as the "master" frame.

At this point we made a digression, to put our reference frame on an absolute basis, even though it is not needed in the present study. The guide-star catalog, and hence the header information, can contain astrometric errors of up to 1.5 arcsec (Koekemoer et al. 2005), so we cross-identified over 6000 of our stars with the 2MASS catalog in order to construct a more accurate absolute astrometric calibration of our reference frame. We found that the 2MASS frame was offset by 0.5 arcsec in declination and 2 arcsec in right ascension from the frame given in the GO-10775 `drz`-frame header. We also found that there was a small orientation difference (0.°1) between the `drz`-based frame and the 2MASS frame. The world-coordinate system (WCS) parameters in the `fits` headers of the stacked images that we provide were constructed to match as well as possible the positions of stars in our frame with those in the 2MASS catalog. Skrutskie et al. (2006) argue that the 2MASS positions for well-measured stars should be good to about 50 mas in a random sense, and good to 15 mas in a systematic sense.

We emphasize that our proper motions do not depend greatly on the quality of our astrometric solution. Each star will be measured relative to its nearby neighbors using only individual flat-fielded (`_flt`) images; the reference frame contributes only to our scale and orientation. Nonetheless, for future use of the catalogs provided here it is still desirable to have the best possible reference frame.

3.2. Image Stack

The transformations from the frame of each exposure into the master frame allow us to generate stacked images of the field in this frame. Our images were generated in a manner akin to `drizzle` with a `pixfrac` parameter of 0 (see Fruchter & Hook 2002). These stacked images provide a simple representation of the field that allows us to independently evaluate how our star-finding algorithms performed (our finding was done on the individual images, not on the stacks).

The stacked images are 14,000 × 14,000 pixels, covering 11.6 arcmin on a side, and were constructed for the F435W, F625W, and F658N filters of GO-9442. We provide these `fits` images as a part of the data release with this paper.

3.3. Constructing the Catalog

Once we had determined a reference frame, we could construct a star catalog in this frame. To do this, we used the same software program that was used for the reductions for the 65 clusters in GO-10775. The details of this program can be found in A08. Briefly, the routine reads in the available images (shallow and deep) for two different filters ($B_{\rm F435W}$ and $R_{\rm F625W}$, in this case) and auxiliary information that allows it to map each exposure into the reference frame, both astrometrically and photometrically. It then goes through the reference frame in patches that are 25 × 25 pixels in size, and identifies all the stars in each patch, measures them, and records their parameters in a file. The routine is able to deal well with short and deep exposures; if a star is saturated in the deep exposures, it is found in the short exposures where possible. It also finds stars iteratively, first finding the bright stars, then removing them to find the fainter stars that might not stand out distinctly in the unsubtracted images. Finally, the routine is robust against identifying PSF artifacts or diffraction spikes as stars.

The GO-9442 data set differs from the typical GO-10775 cluster data set. Here, the master frame was 14,000 × 14,000 WFC pixels in size, and consisted of a mosaic of pointings, whereas in the GO-10775 set, the observations consisted of medium-sized dithers about one central pointing and could fit comfortably within a 6000 × 6000 pixel region. The typical point in the field under study here had coverage of 3B and 3R observations. In order to be included in the catalog, we insisted that a star be found in at least four out of these six observations independently; if there were fewer exposures available at a given point in the field, the criteria were relaxed accordingly (see A08).

The automated finding program identified 1,164,317 stars in the $B_{\rm F435W}$ and $R_{\rm F625W}$ images. We plotted the star lists on top of the stacked images to verify that the routine had identified all the stars we expected it to. This inspection confirmed that there were very few stars that were missed by the automated routine. The few missed stars fall into two classes: medium-brightness stars in the vicinity of saturated stars, and blended pairs of stars that had one star that was brighter in $B_{\rm F435W}$ and the other brighter in $R_{\rm F625W}$. The former were passed over by the program because they were too likely to be artifacts near saturated stars, and it was better to err on the side of caution. The latter were missed because we required each star to be found as a dominant peak in at least four independent images. Both of these loss mechanisms can be quantified with artificial-star (AS) tests (see below).

To get an idea of how many real stars were missed, we ran the same finding program on the F658N images (which had less saturation and four exposures at each pointing), requiring a star to be found in at least three out of four exposures, and cross-identified the stars in the two catalogs. There were about 30,000 stars (3% of the total) that were found in the Hα images that were not found in the $B_{\rm F435W}$ and $R_{\rm F625W}$ observations. We looked at where these missing objects were located, and they were almost exclusively found in the situations detailed above.

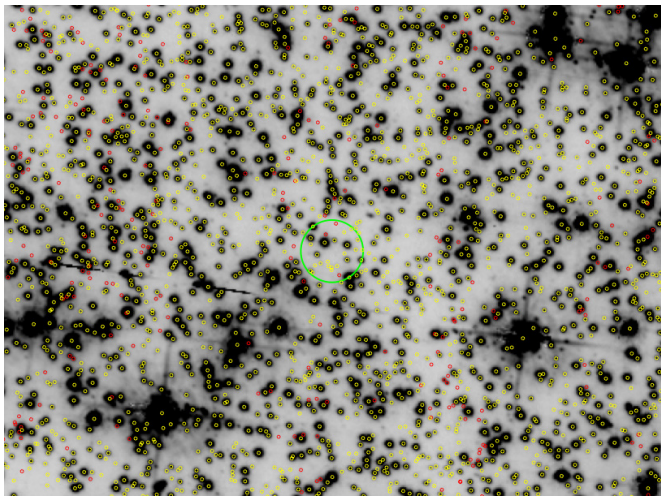

Figure 2. Stack of the deep F625W images at the center of the cluster. The yellow circles identify the stars found in the B_{435} + R_{625} list. The red-circled stars were found in the H_{658} list, but not the B_{435} + R_{625} list. The large green circle is the location we have identified for the center (see Section 4). The field shown is 21″ × 16″.

In Figure 2, we show the central region of the cluster. The stars found jointly in $B_{\rm F435W}$ and $R_{\rm F625W}$ are marked in yellow. The stars that were found in $H_{\rm F658N}$ (Hα) but not in $B_{\rm F435W}$ and $R_{\rm F435W}$ are marked in red. Of course it would be good to have a list that contains every single star in the cluster, but a compromise must always be made between including the marginal star and including image artifacts as stars. There will always be stars that are missed; the important thing is to be able to quantify this incompleteness.

3.4. Calibrating the Photometry

The fluxes for the stars measured in the above routine are reported in instrumental magnitudes, $-2.5\log_{10}Z$, where Z is the scaling that matches the effective PSF model to the stellar profile. The PSF model was normalized to have a flux of 1.00 within a radius of 10 `_flt` pixels. The short exposures have been zero-pointed to match up with the deep exposures, therefore the task of calibration simply involves determining the zero point that will bring the instrumental photometry of the deep exposures into the VEGAMAG system.

Since the GO-9442 data set has already been calibrated by Villanova et al. (2007), we simply adopted the photometric zero points from that project. They are $\rm ZP_{F435W} = 32.043$, $\rm ZP_{F625W} = 31.991$, and $\rm ZP_{F658N} = 28.904$. Figure 3 shows our ($B_{\rm F435W} - R_{\rm F625W}$) color–magnitude diagram (CMD) in both the instrumental and in the calibrated systems. We will continue to report many of the analyses here in the instrumental system, since it is easier to assess errors in terms of signal-to-noise ratio (S/N) when working directly in photoelectrons. For reference, saturation in the deep images sets in at an instrumental magnitude of around −13.75, and a star with a magnitude of −10.00 has an S/N of 100. In the rest of the paper, when referring to the instrumental system, we will report magnitudes as $m_{\rm F435W}$, and when referring to the calibrated VEGAMAG photometry, we will refer to $B_{\rm F435W}$.

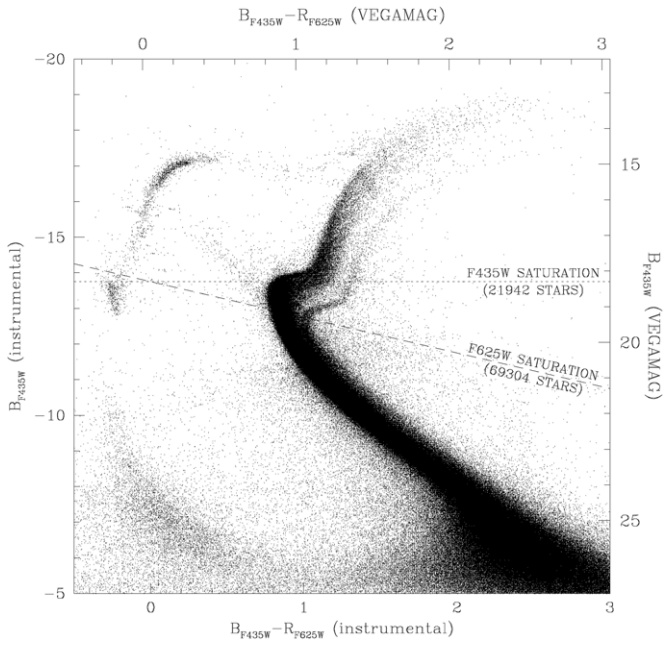

Figure 3. CMD of all the stars found in the automated search of the F435W and F625W exposures of GO-9442. The level where saturation sets in for the deep exposures is indicated, as well as the number of stars that are saturated. Most of the stars above the deep-image saturation line were measured well in the short exposures. Saturation in the short exposures sets in at about 4 mag brighter than this. These particularly bright stars were measured by fitting the PSF to the unsaturated part of the star's profile. Note the multiple MS turnoffs, which have been well discussed in the literature (i.e., Ferraro et al. 2004; Villanova et al. 2007).

3.5. Artificial-star Tests

The GO-9442 images are not terribly crowded. There are about 1.2 million stars in 14K × 14K pixels, thus the typical separation is about 10 pixels. Nevertheless, the fact that there are quite a few extremely bright stars makes it impossible to find all the faint stars. And even though the density changes by less than a factor of 4 from the center to the corners of the field, it is still important to have an idea of the completeness for each brightness level of star at different places within the field. Therefore, we decided to run AS tests in order to gauge the incompleteness and measurement quality.

The mechanism for AS tests is described thoroughly in A08. Briefly, since our finding software operates on one small patch of the field at a time, we can afford to do AS tests in serial, one at a time, rather than doing them in parallel in many batches. One great benefit of this is that artificial stars never interfere with each other, so by throwing many stars in successively we can simulate throwing in a high density of them. This makes it easy to do a detailed study of the completeness in the vicinity of the center.

We performed 500,000 individual AS tests. For each, we chose a random F435W instrumental magnitude between −14 (saturation) and −5, and chose the F625W magnitude that placed the star along the fiducial MS. The artificial stars were inserted with a flat distribution in radius, so that we would probe the central regions more than the outer regions. For example, we ended up inserting over 700 stars within the central arcsecond in radius, and over 51,000 stars within the central 10 arcsec.

As a demonstration of how the AS tests worked, in Figure 4 we show the same central field as in Figure 2, and the locations where the artificial stars were and were not recovered. In this region, we observed 261 real stars between −10.5 and −11.5 in F435W instrumental magnitudes. We ran 3847 AS tests in this magnitude range over this 225 square arcsecond region, and recovered 3402 of them, resulting in a completeness of 88%.

Figure 5 shows the results of the AS tests for different radial bins as a function of instrumental magnitude. It is clear that the completeness at the center is well over 90% for the brightest stars, and is over 75% throughout the cluster for stars with instrumental magnitudes brighter than −10, which corresponds to stars about 4 mag below the upper sub-giant branch (SGB).

3.6. Measuring the Proper Motions

Figure 1 shows that proper motions can be measured in two fields: one field that is largely centered on the cluster and another that is east SE of the center by about 4 arcmin. Table 1 lists the observations we have available for each field.

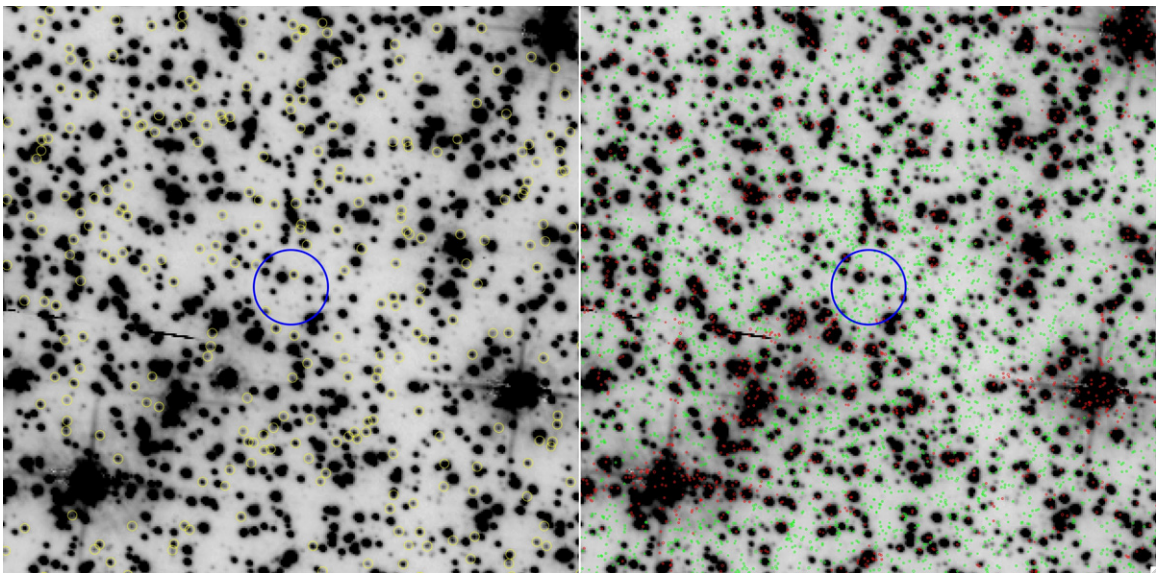

Figure 4. Central swath of the stacked image (15″ × 15″ in each panel). On the left, the yellow circles indicate stars that were found between −10.5 and −11.5 (in F435W instrumental magnitudes). On the right, we show where stars in the same brightness range were successfully recovered from our AS tests (green), and where they were not recovered (red). The center (determined in Section 4) is shown in both panels with a blue 1″ radius circle around it.

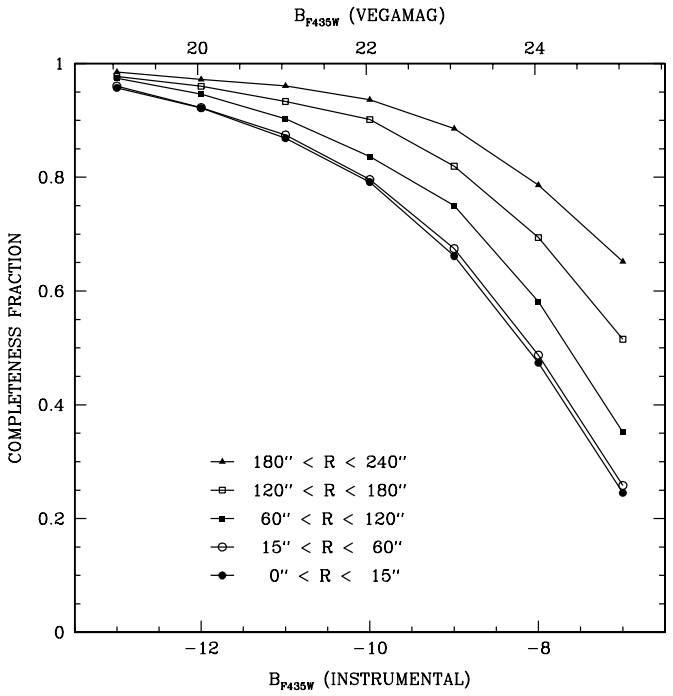

Figure 5. Completeness as a function of magnitude for stars at different distances from the cluster center.

Our procedure for measuring proper motions was to measure the stars individually in each exposure for each epoch, and then to combine the many independent measurements to construct proper motions for the stars that can be found in multiple epochs. The agreement among the many independent observations for each star at each epoch gives us a handle on the errors in the positions, and hence in the displacements and proper motions.

The GO-10252 images are well matched depthwise to the GO-9442 images, thus we should expect the same stars to be measured equally well in both epochs. By contrast, the GO-10775 images, which cover the central field, are a factor of 4 shallower than the GO-9442 data set, and therefore have different S/Ns for the same stars.

3.6.1. Measuring the Star Positions

The first step in determining proper motions is to measure an accurate position for each star in each individual exposure at each epoch. To do this, we once again ran the star-measuring program `img2xym_WFC.09x10` to construct a list of sources in each exposure, using empirically determined PSFs with a spatially constant perturbation to account for breathing-related focus changes from exposure to exposure.

The routine produced a list of positions and instrumental magnitudes for the reasonably bright and isolated stars identified in each exposure. Since our aim was to include only the unsaturated stars that could be measured accurately, we adopted finding parameters such that we would find unsaturated stars with at least 250 counts in their brightest 4 pixels and with no brighter neighbors within 4 pixels. We also confined our attention to the deep exposures for each filter/epoch combination, since there is generally only one short exposure at each location and it is hard to get a good handle on astrometric errors without multiple exposures. Finally, we treated the central and adjacent major-axis proper-motion fields separately, since there is only marginal overlap between them.

3.6.2. The Central Field

For the central field, we have 10 exposures in the first epoch in filters $B_{\rm F435W}$, $R_{\rm F625W}$, and $H_{\rm F658W}$, and eight exposures in the second epoch in filters $V_{\rm F606W}$ and $I_{\rm F814W}$. We reduced each exposure as described above, producing a list of x, y, and m (instrumental magnitude) for each one. We treated the two WFC chips for each exposure independently, so we had a total of 36 lists of stars, one for each chip in each exposure. We corrected the positions for distortion and cross-identified each list with the reference-frame list, allowing us to develop a least-squares linear transformation from each exposure into the reference frame. Since the central field covers only a fraction of the GO-9442 field, we restricted ourselves here to the subset of 422,561 stars contained within the region [4000:9999,4000:9999].

The above linear transformations yielded an estimate for the reference-frame position for each star from each exposure in which it was found. These global transformations can contain some small systematic residuals, due to variations in the distortion solution caused by breathing or other effects. The consequence of these errors is that the transformed positions for the stars in one part of the reference frame are all shifted by some (small) amount. In order to remove these residual transformation artifacts from the data, we determined a local adjustment for each observation of each star as follows. We first identified all the neighboring stars within a 100 pixel radius that were unsaturated and had an S/N > 40 (excluding the target star itself). For each exposure where the star was observed, we then found a robust average offset between the globally transformed positions of the neighbor stars for that exposure and the average reference-frame positions for the stars. This average offset provided the correction to the transformed position of the target star for that exposure.

Figure 6 shows the residuals before and after this correction for the first image for each epoch. The typical adjustment is 0.01 pixel, which is about the accuracy that we expect for the static distortion solution (Anderson 2005). But not all of this adjustment comes from static distortion-solution error; much of it clearly varies from exposure to exposure due to breathing-related changes in focus. The effect of this correction (and, indeed, of the star-based transformations themselves) is that the motion of each star is measured relative to that of the average motion of its neighbors. Since outliers are rejected in the process of determining the average motion of the neighbors, this means that each star's motion is computed relative to the bulk cluster motion at its location. Section 3.6.4 discusses what this calibration procedure means in practice for the motions that we measure.

At this point, we had in-hand corrected reference-frame positions for a large number of stars measured in a large number of independent exposures. We combined the data in several ways. First, for each filter/epoch combination, we averaged all the data together to arrive at an average position, magnitude, and rms error for each star. We also combined the astrometric data together by epoch. (Since the F658N data have a lower S/N at the faint end, we include F658N astrometry only when the star had an instrumental magnitude of $H_{\rm F658N} < -10$, indicating an S/N of 100.)

The proper-motion results for the central field are illustrated in Figure 7. Each data set consisted of three to four observations of each star. We constructed an average reference-frame position for each star in each data set, then computed the error in this position from the rms about this average. The two-dimensional

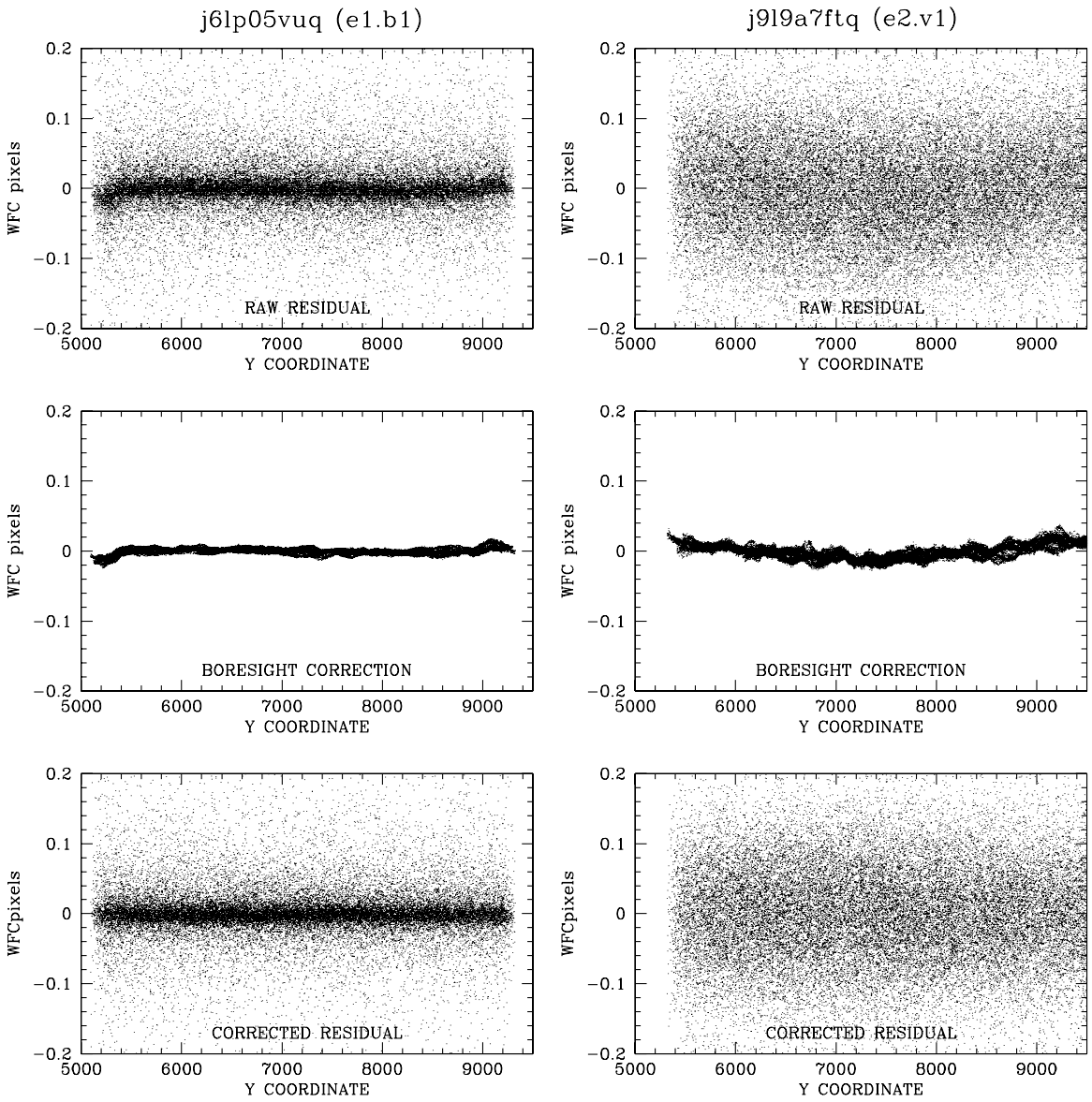

Figure 6. Left: in the top panel, we show the *x*-residual between the first F435W image in GO-9442 (`j6lp05vuq`) and the reference frame for a 100-pixel-tall strip through the cluster center. Since the reference frame is based on images taken at that epoch, these residuals should show just distortion errors and should have no proper motions. The middle panel shows the local "boresight" correction used for each star. The bottom panel shows the residuals after the local adjustment. Right: same, but for the first exposure in the second epoch (`j9l9a7ftq`). These residuals contain both distortion errors *and* actual proper motions, and therefore show more scatter than in the left panels.

error in the average position at a single epoch is typically 0.01 pixel. This error was achieved for the data set for each filter at each epoch.

The proper motions were constructed by subtracting the first-epoch positions from the second-epoch positions and dividing by the time baseline. The multiple data sets we had at each epoch allowed us to construct two independent observations of the proper motions. We constructed one displacement comparing the second-epoch F606W positions with the first-epoch F435W positions, and a second displacement by comparing the second-epoch F814W with the first-epoch F625W. The top panels of Figure 8 compare these two independent measurements. The distribution along the 45° direction represents the actual motion measured, found to be the same in both halves. The distribution in the 135° direction represents the error in our measurements. The typical displacement between epochs is about 0.15 pixel. The displacement of the typical star is measured with a fractional error of less than 10% (from the aspect ratio of the distributions in the upper panels).

We combined all the data for each epoch and constructed a single proper motion for each star, which we plot in the lower panels as vector-point diagrams. There are very few outlier stars, meaning that we have done a good job selecting stars with small errors. It is worth pointing out that our finding criteria have not selected against high-motion stars: the field stars in this diagram demonstrate that we are finding stars with displacements of up to 1 pixel. Thus, we are clearly sensitive to cluster members with more than 10 times the typical motion. The baseline for this central field is 4.07 yr, thus a displacement of 0.08 pixel corresponds to about 0.02 pixel per yr in each coordinate, or 1 mas yr^{-1}.

We measured proper motions for the 108,507 stars that could be found in at least two images of each epoch, with an rms of position measurements within each epoch of less than 0.03 pixel

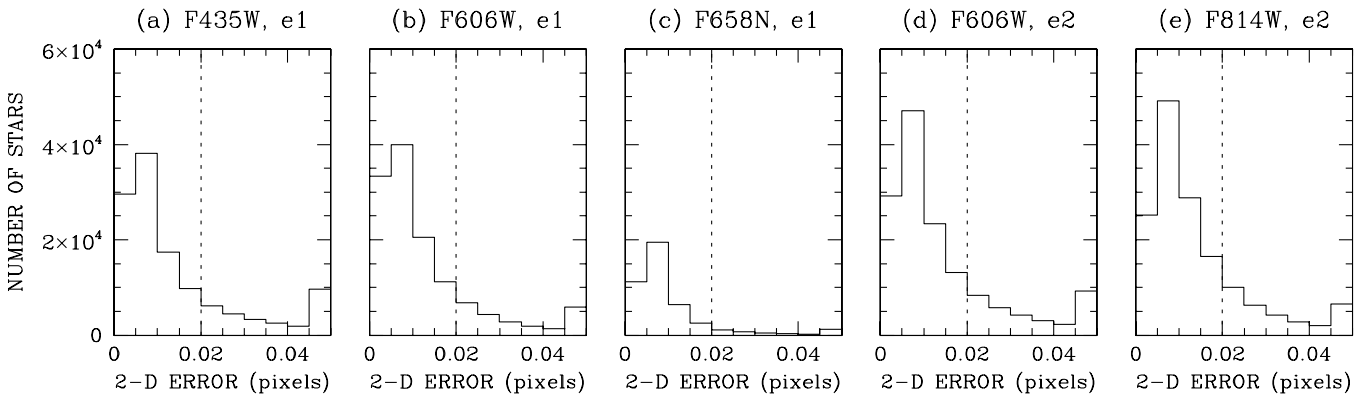

Figure 7. Panels (a)–(c) show the distribution of $\sqrt{\sigma_x^2 + \sigma_y^2}$, the total two-dimensional error in the position for the first-epoch F435W, F625W, and F658N data, respectively. This error was computed by taking the rms of the scatter among the multiple observations of the master-frame position for each star and then dividing by the square root of the number of observations. The dotted line drawn at 0.02 pixel indicates the boundary between the well and poorly measured stars. Panels (d) and (e) show, respectively, the same for the F606W and F814W data of the second epoch.

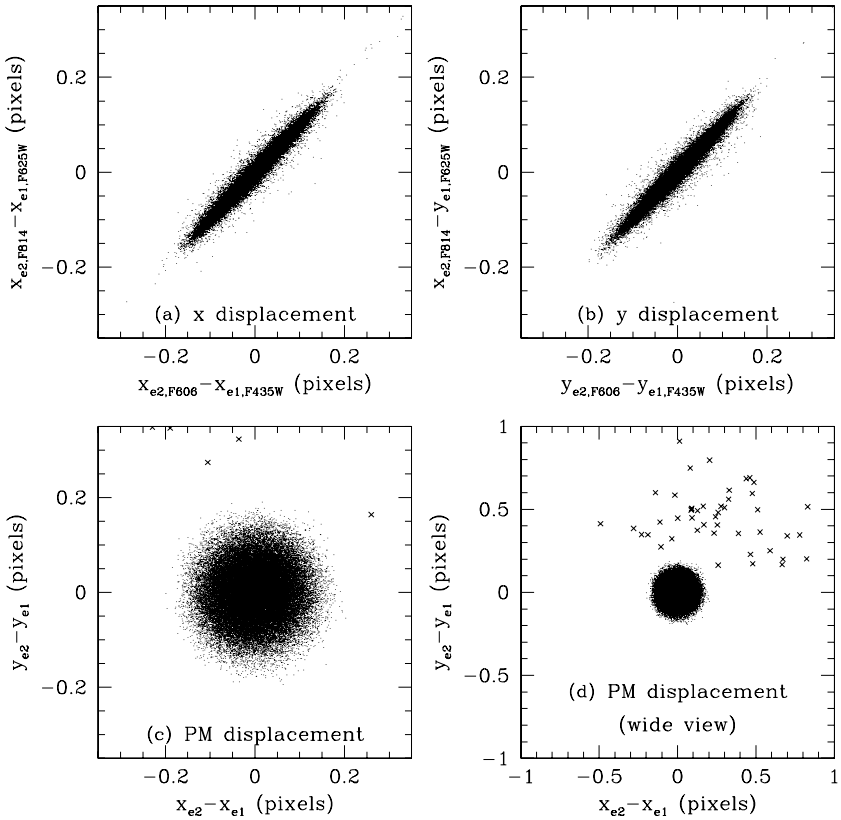

Figure 8. Panel (a) compares two independent measurements of the x displacement between epoch 2 and epoch 1. The agreement between the two is an indication of the quality of the proper motions. Panel (b) shows the same for the y displacement. Panel (c) shows the resulting two-dimensional displacement distribution, after combining the data from all filters for each epoch. Panel (d) zooms out to show the cluster and field stars (points beyond 0.25 pixel are displayed as crosses for clarity). The time baseline between these epochs is 4.07 yr. The pixel scale is 50 mas pixel^{-1}, and the x-axis of the reference frame is aligned with the negative right ascension axis.

(per coordinate). In addition, we defined a "high-quality subset" of the data that should have more uniform proper motion (PM) errors by selecting those stars for which this position rms was less than 0.02 pixel and for which the instrumental $m_{\rm F435W}$ photometry was brighter than -11. Figure 9 shows a CMD of the stars that qualify for the high-quality subset. Our high-quality motions are limited to stars on or below the SGB and those brighter than $m_{\rm F435W} = -11$, a few magnitudes below the turnoff. Stars much brighter than the SGB were saturated in the deep GO-10775 exposures. Most of the proper-motion analysis in this paper and Paper II will use this high-quality sample of 53,382 stars. Within this sample, the typical proper-motion error is better than 0.1 mas yr^{-1} in each coordinate, corresponding to 0.008 pixel over the four-year baseline. Over the magnitude range where we could measure reliable motions, we measured between 80% and 90% of *all* the stars.

3.6.3. The Adjacent Major-axis Field

In a similar way to that described above, we constructed proper motions for the adjacent field along the major axis. Since the GO-10252 data straddled two of the GO-9442 pointings, we had to use two first-epoch pointings here, which doubled the

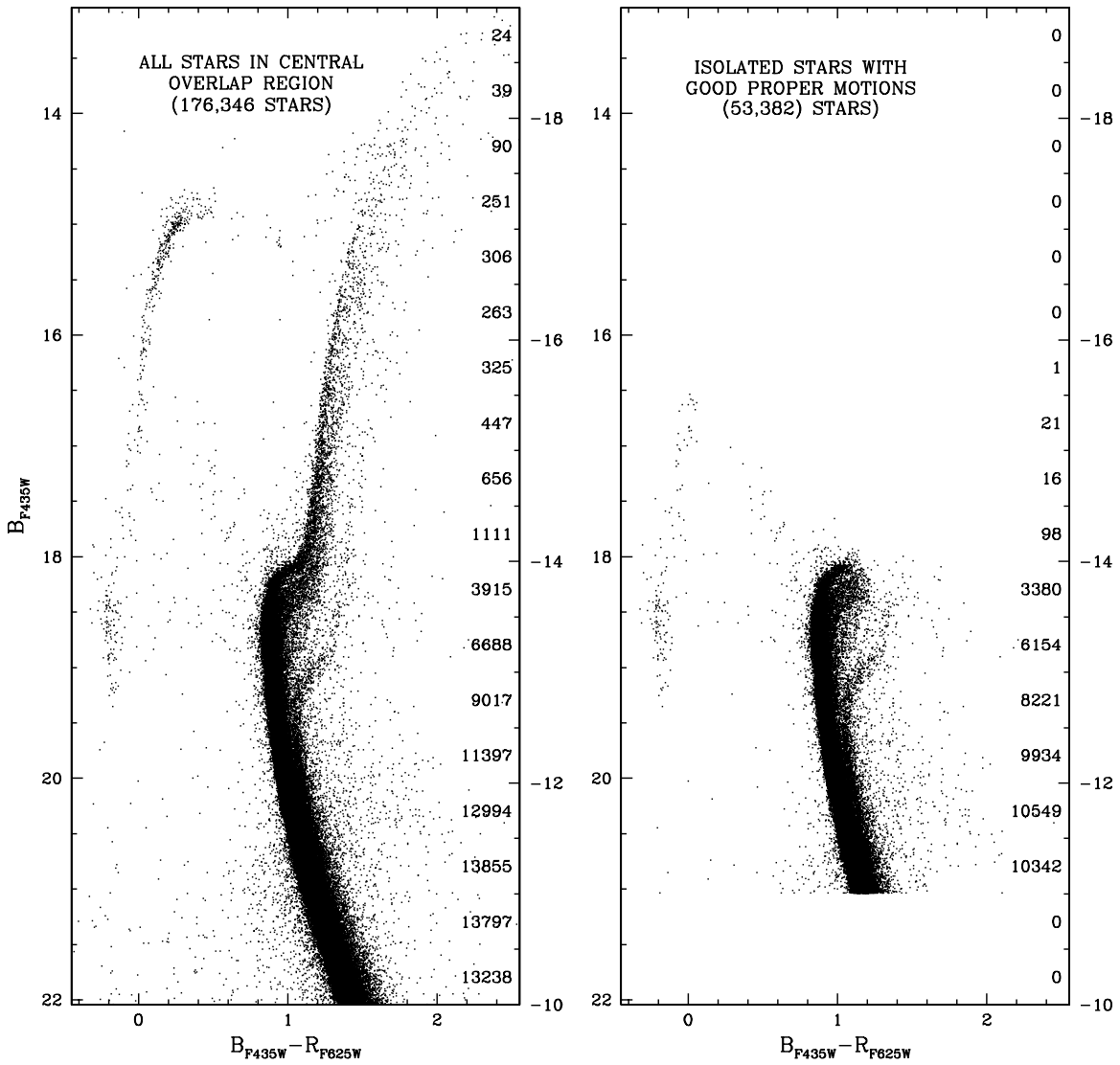

Figure 9. Left: all the stars from the catalog in the region of overlap between the central pointing of GO-9442 and GO-10775. Right: the stars found to have reliable proper motions. On the right of each CMD, we add up the number of stars in each 1 mag bin.

number of exposures to handle, but the overall reduction was generally the same. To qualify for this proper-motion catalog, we required that a star be found in at least four first- and four second-epoch exposures. (Because of possible distortion errors at the edges of the out-of-focus GO-10252 data set, we insisted on a star being found in at least four exposures to ensure that the internal errors will be able to indicate when stars have distortion issues.)

We found 61,293 stars for which we could measure proper motions in the adjacent field. As above for the central field, we defined a high-quality sample of stars that should have uniformly good motions. To qualify for this sample, a star had to have an rms of measurements within each epoch of less than 0.02 pixel, and had to be brighter than $m_{\rm F435W} = -11$. The high-quality proper-motion catalog for the adjacent field contains 19,593 stars.

3.6.4. Proper-motion Zero Points

The proper motions we have measured here are not absolute proper motions, as is generally true for other GCs observed with *HST* (see McLaughlin et al. 2006 for a broader discussion). *HST* can measure absolute proper motions only when it has absolute reference points to measure displacements against. The Omega Cen fields are so crowded that there are no detectable galaxies that could serve as absolute reference points. Also, the stability and repeatability of *HST* (while superb) are not sufficient to compare different frames directly. For example, there are small changes in focus due to temperature-induced telescope breathing. These cause scale changes that need to be calibrated out. Moreover, the nominal orientation (roll) repeatability of *HST* is $0\overset{\circ}{.}003$. If left uncalibrated, this would induce apparent solid-body rotation of the cluster that exceeds the internal motions. Hence, to be able to derive relative proper motions, we need to use general six-parameter linear transformations to match exposures to each other.

The application of linear transformations implies that scale, rotation, two skew terms, and two translation terms cannot be measured from the data. The removal of scale and skew terms is not an issue, because the dynamics of a cluster in equilibrium do not display time variability in these terms. The translation terms imply that we cannot measure the mean motion of Omega Cen with respect to the Sun. This does not affect the internal cluster dynamics, which is our primary concern here. Therefore, the only important fact to keep in mind is that all proper motions

reported here are measured modulo an undetermined solid-body rotation component. We show in Section 5.2.3 of Paper II that this does not impact our modeling. Ground-based line-of-sight studies of Omega Cen reported by van de Ven et al. (2006) show that any true solid-body rotation in our central field should be quite negligible, even though we cannot measure it directly here. Note in this context that any unaccounted for solid-body rotation component would generally tend to *decrease* the IMBH mass implied by models, since it would act to lower the kinematical gradient between the inner and outer parts of the cluster.

To be able to remove small time variations in high-order geometric-distortion terms, we have gone one step further in our calibration. Namely, we measured each star relative to its local neighbors (see Section 3.6.2). All the neighbors used should be moving with the cluster, but each will have some random internal motion. We measured each star against hundreds of its neighbors, so the random internal motions should average out. Therefore, the proper-motion zero point is different for each star, and equals the mean projected motion of cluster stars at its position on the sky. In other words, all mean motion is removed, not just solid-body rotation.

The "local-neighbor correction" procedure allows the most accurate measurement of the internal proper-motion dispersions for the cluster. However, this correction is applied by choice, and not by necessity. We would not want it to remove an important signal that is in fact present in the data. Mean motion in the radial direction should not exist in an equilibrium cluster. However, there could be differential rotation (i.e., the part of the rotation curve that is not a linear function of radius). A Keplerian rise in rotation around an IMBH would fall in this category. There is no evidence for such differential rotation in any existing data, but we can verify this directly with our *HST* data. Without the local-neighbor corrections, the data are fully sensitive to small-scale internal rotations and motions.

Figure 10 visualizes the size of the local-neighbor corrections that were applied. Our sets of stars with good proper motions were distilled into boxes 100 pixels on a side. We computed the proper motion for each star two ways. First, we took the estimate generated above, which involved removing from each position measured in each image the average of the local neighbors. Second, we skipped this "boresight" correction, using only six-parameter global linear transformations to relate positions in each image to the master frame. The difference between these two measured positions is shown as the vector in the plot. A vector that reaches the edge of the circle corresponds to a displacement difference of 0.01 pixel.

The vectors in Figure 10 correspond to the mean local motions that were subtracted. Two things are evident. First, the corrections are very small. The typical adjustment is less than 0.01 pixel, which is characteristic for geometric-distortion residuals. This corresponds to about an eighth of the observed proper-motion dispersion, and is too small to have dynamical importance for the cluster. Second, there is no overall rotation pattern visible. The correction field is patchy and incoherent. Again, this is as expected for geometric-distortion residuals, and this cannot be due to internal motions of the cluster. More specifically, there is no excess rotation near the cluster center that would be typical for Keplerian rotation around an IMBH.

As a further check, we also used the methods of Paper II to determine the rotation curve (mean tangential proper motion as a function of radius) for the proper-motion catalogs with and without the local correction. The difference in rotation curves was less than 1 km s^{-1} at all radii in the central field.

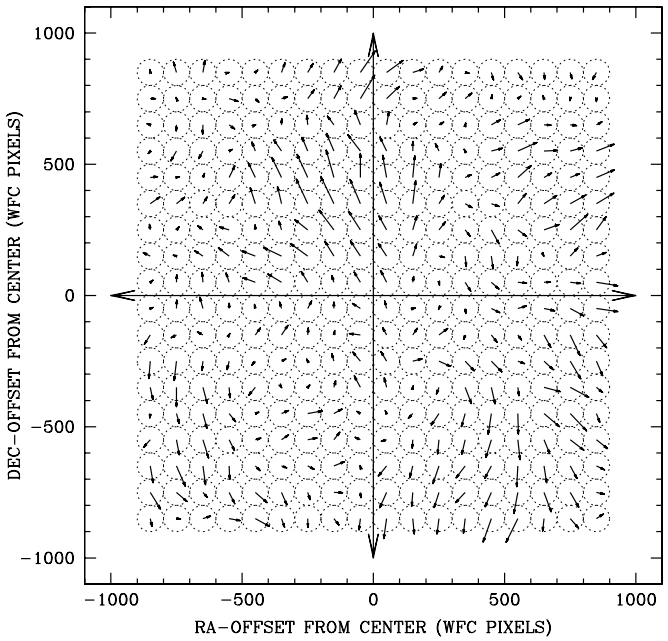

Figure 10. Illustration of the average local corrections applied when deriving the proper motions, as a function of position. The average vectors were derived as described in the text for 18 × 18 bins that cover the inner 1.′5 × 1.′5. Vectors that extend to the edge of the circle correspond to a displacement difference of 0.01 pixel, which is typical of geometric-distortion residuals. The size of the corrections is too small (approximately one-eighth of the rms cluster motion) to have any dynamical influence. The morphology of the vector field indicates that we are not inadvertently removing rotation intrinsic to Omega Cen.

In summary, our catalog formally contains proper motions after subtraction of all mean motion in the plane of the sky. However, detailed analysis and ground-based data indicate that any mean motion that the cluster may in fact possess is dynamically irrelevant at the central-field radii of our *HST* study.

In Sections 6 and 7, we present an initial analysis of the proper motions. Paper II will combine these motions with existing proper-motion, radial-velocity, and surface-profile data from the literature and will construct comprehensive dynamical models for the cluster.

3.7. Catalog and Image Products

In the previous sections, we described how the WFC images were analyzed to construct star and proper-motion catalogs. These catalogs are available along with the online version of this paper.

Specifically, we have analyzed the 10′ × 10′ field of data set GO-9442, which goes out to beyond two core radii. We have one table that contains 1,164,317 stars found from running our automated finding algorithm on the F435W and F675W images.[1] Table 2 gives the column-by-column description of this file. These measurements can be converted to calibrated photometry using the zero points included in the table (from Section 3.4). We also provide the `fits` images referred to in Section 3.2, which contain a WCS header and which are in the same coordinate system as the star catalogs.

[1] Upon careful inspection of our bright stars, we found 112 bright stars spread throughout the field in the initial catalog that were actually detector artifacts along the bleed pixels of extremely bright saturated stars. We identified these stars easily as they had no counterpart at all in the Hα or the short images, thus we have removed them from our catalog. This is the only non-automated aspect of our catalog.

Table 2
Columns in the Star Catalog and in the Artificial-star-run Catalog

Column	Description
1	x position in the reference frame
2	y position in the reference frame
3	$m_{\rm F435W}$, instrumental B magnitude, $\rm ZP_{VEGA} = 32.043$
4	$m_{\rm F625W}$, instrumental R magnitude, $\rm ZP_{VEGA} = 31.991$
5	rms scatter of the single-exposure x positions
6	rms scatter of the single-exposure y positions
7	rms scatter of the single-exposure $m_{\rm F435W}$ observations
8	rms scatter of the single-exposure $m_{\rm F625W}$ observations
9	Number of B images where star could have been found
10	Number of B images where star was found well
11	Number of R images where star could have been found
12	Number of R images where star was found well

Notes. Columns 3 and 4 give instrumental magnitudes, which can be transformed to the VEGAMAG scale by addition of the listed zero points $\rm ZP_{VEGA}$. Stars brighter than about −13.75 are saturated in the deep exposures, and therefore have larger systematic errors. We report the rms scatter in individual observations of each star. In principle, the errors in Columns 1–4 can be constructed by dividing these rmss by the square root of the number of observations (Columns 10, 12, or their sum). However, not all errors are random, so this may underestimate the errors. The rms can be used to help select stars with good measurement consistency.

(This table is available in its entirety in a machine-readable form in the online journal. A portion is shown here for guidance regarding its form and content.)

Table 3
Columns in the Input Parameters for the Artificial-star Tests

Column	Description
1	Input x position in the master frame
2	Input y position in the master frame
3	Input instrumental F435W photometry
4	Input instrumental F625W photometry
5	Number of deep F435W images the star could have been found
6	Number of deep F625W images the star could have been found
7	Number of short F435W images where star could have been found
8	Number of short F625W images where star could have been found

(This table is available in its entirety in a machine-readable form in the online journal. A portion is shown here for guidance regarding its form and content.)

We also ran 500,000 AS tests and subjected them to the same finding and measuring algorithm as was used on the real stars. These tests are also reported in the table, which is also available in its entirety with the online article. The AS tests report the same measurement quantities as in Table 2 for the real stars; but for the AS tests, we also have the input positions as well (see Table 3). It is worth pointing out that just because something was "found" in an AS test, that does not mean that the input star was actually recovered; it is important to compare the input and output positions and fluxes to determine that the inserted star, and not a brighter pre-existing neighbor, was indeed recovered.

Finally, we provide the proper-motion measurements in separate files for the central and major-axis fields. The central field has motions for 108,507 stars and the adjacent major-axis field for 61,293 stars. Table 4 gives a column-by-column description of the proper-motion data. The "good" flag refers to stars that are part of the high-quality subset defined in Section 3.6.2, which is used in the later sections of this paper and in Paper II.

Table 4
Columns in the Proper-motion Catalogs

Column	Description
1	x position in the reference frame
2	y position in the reference frame
3	$B_{\rm F435W}$, calibrated VEGAMAG B magnitude
4	$R_{\rm F625W}$, calibrated VEGAMAG R magnitude
5	μ_x, proper motion in x, mas $\rm yr^{-1}$
6	μ_y, proper motion in y, mas $\rm yr^{-1}$
7	σ_{mu_x}, proper-motion error in x, mas $\rm yr^{-1}$
8	σ_{mu_y}, proper-motion error in y, mas $\rm yr^{-1}$
9	$\mu_{\rm maj}$, proper motion along major axis
10	$\mu_{\rm min}$, proper motion along minor axis
11	$N_{\rm e1}$, number of exposures with good positions in epoch 1
12	$N_{\rm e2}$, number of exposures with good positions in epoch 2
13	g, the "good" flag, indicating small internal errors

Notes. The proper-motion errors are determined by adding the errors in the average for each epoch in quadrature, assuming no inter-epoch transformation error. The major/minor-axis projections were made assuming the major axis to be 100° east of north.

(This table is available in its entirety in a machine-readable form in the online journal. A portion is shown here for guidance regarding its form and content.)

In the following sections, we will use these catalogs to determine the center of the cluster (Section 4), to extract a surface-density profile (Section 5), and to search for a cusp in the velocity distribution that could be indicative of an IMBH at the center (Section 6). Finally, in Section 7, we will compare the proper motions for stars in different populations.

4. DETERMINING THE CENTER

In general, the center of a cluster can be determined to a precision of about $\sigma/\sqrt{N}$, where σ is roughly the core radius and describes the falloff of the spatial distribution, and N is the number of stars used in the center determination. For a cluster like Omega Cen, which has a core radius of 2.′5 (150″), this means we would need over $150^2 = 25{,}000$ stars to measure a center to within an arcsecond. These stars would have to be spread out to well beyond a core radius to give us a good handle on the center. (The center is defined as much by where stars are *not* as by where they are.)

In the case of a Gaussian distribution, the most accurate way to measure the center is in fact to take a simple centroid of the star positions. However, there are several factors that can complicate this simple solution. For example, if the region surveyed is not symmetric with respect to the center, then we must include some correction for this effect on the centroid. Similarly, if the list of stars used in the determination is not complete throughout the field, then we must consider how this will affect the center determination. The presence of bright giants can prevent us from finding the more plentiful MS stars in their vicinity, and the small-number statistics of the giants' distribution can result in patchy incompleteness. All these limitations can be overcome; but it is important to address the issues carefully.

In this section, we employ several different ways of determining the center from our data. We determine the density center from star counts, and the kinematic center from proper motions. In both cases, we use two separate methods to find the point of symmetry: one based on contours and the other based on pie slices. As an independent cross-validation, we also derive the

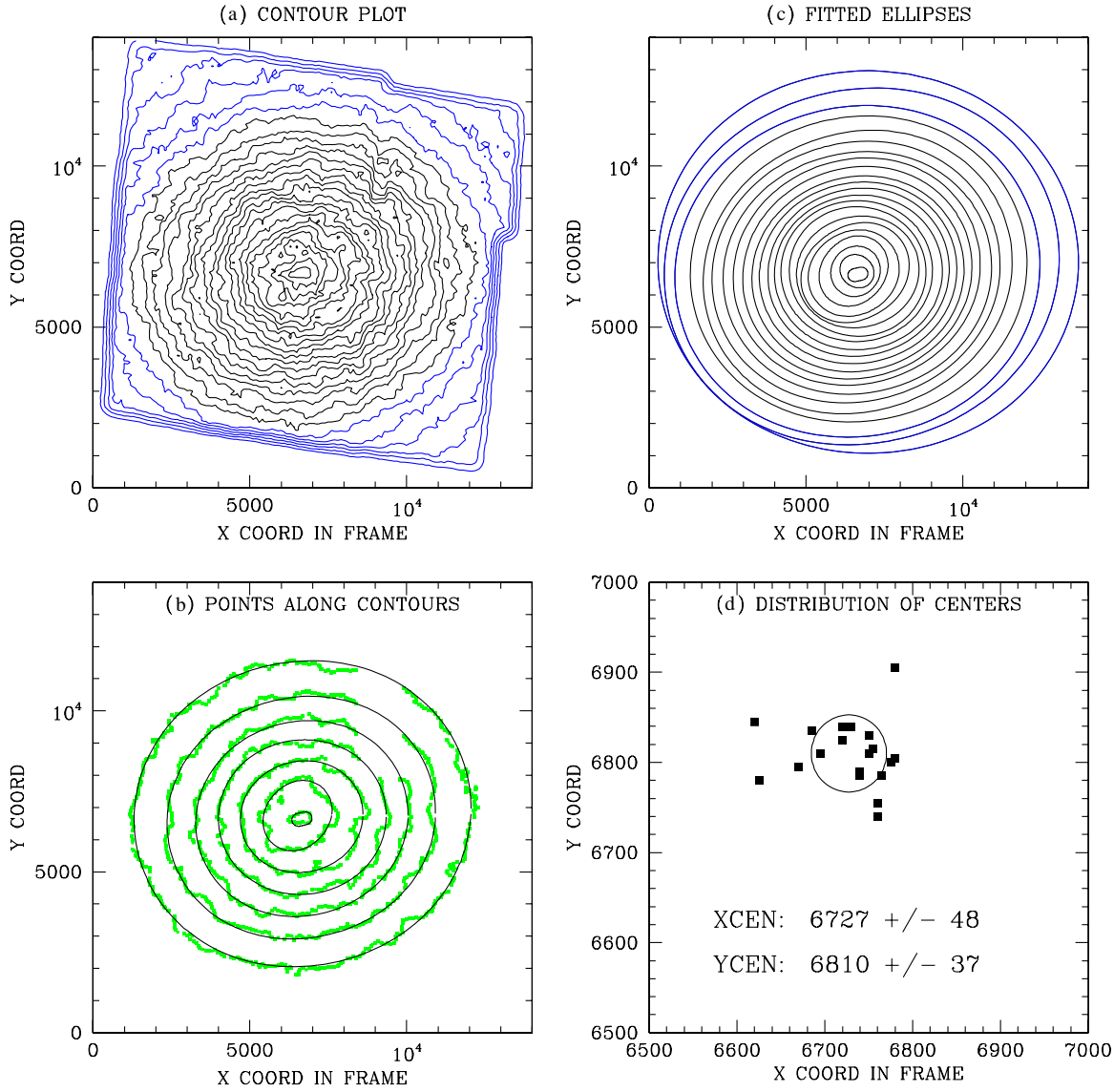

Figure 11. Panel (a): the isodensity contours for all stars with $m_{F435W} < -9$. Contours are separated by 100 stars (per $25'' \times 25''$ box). The blue contours are contaminated by the edges of the field and are not used. Panel (b): the points along contours 700, 1000, 1300, 1600, 1900, 2200, and 2500, and the ellipses that were fitted to them. Points in the gap region in the northwest were not used. Panel (c): the fitted ellipses (the parameters are given in Table 5). Panel (d): distribution of the ellipse centers. The circle is centered on the average and has a radius equal to the rms of observations about the average. This rms is also listed in the panel. The uncertainty in the average position is smaller by $\sqrt{N}$, where $N \gtrsim 4$ is the number of *independent* contours.

(A color version of this figure is available in the online journal.)

center of unresolved cluster light in a 2MASS mosaic image of the cluster. We find that all methods yield centers that agree to within the calculated errors. We compare these centers with previous determinations available in the literature.

4.1. Isodensity-contour Centroids

The first way in which we determined the center was by constructing isodensity contours, and fitting ellipses to them. We began by sifting the stars in our 14,000 × 14,000 pixel reference frame into an array of 140 × 140 bins, where each bin is 100 × 100 pixels ($5'' \times 5''$). We found that these bins did not contain enough stars to generate smooth contours, so we subsequently overbinned the distribution, making each bin correspond to 500 × 500 pixels, or ($25'' \times 25''$).

The upper-left panel of Figure 11 shows the contours for the stars with $m_{\rm F435W} < -9$. The edges of the field are clear, as is the region north of (9000, 8000) where there is a gap in the coverage (see Figure 1). Our aim was to fit ellipses to the valid parts of these contours. The contours traced in black are the ones that we trusted to be far enough from the edges of the field to be valid.

In panel (b), we show the points that fall along every third contour (for clarity), and the ellipse that we fitted to each. In these fits, along each contour we used only the points that were well away from the gap region. Panel (c) shows the ellipses fit to all the contours. The parameters of the fitted ellipses are given in Table 5.

Panel (d) in Figure 11 shows the centers of the contours shown in panel (c). The average position for the center is (6727,6810) with an rms of about 45 pixels in each coordinate. Since the contours are not entirely independent of each other, we cannot simply construct an error in the center by dividing the rms by the square root of the number of contours fit. However,

Table 5
Summary of the Fitted-ellipse Parameters for the Contours from Stars Brighter than $B_{435} = -9$

Density	Fitted Center	$\frac{1}{2}(B+A)$	P.A.	B/A
700	6780 6905	5055	100	0.87
800	6750 6810	4648	108	0.86
900	6695 6810	4320	104	0.86
1000	6740 6785	4018	102	0.86
1100	6720 6825	3726	106	0.87
1200	6740 6790	3471	106	0.88
1300	6760 6755	3207	104	0.88
1400	6765 6785	2982	102	0.89
1500	6780 6805	2749	102	0.89
1600	6775 6800	2539	96	0.89
1700	6720 6840	2303	92	0.90
1900	6755 6815	1841	102	0.87
2000	6670 6795	1618	118	0.80
2100	6625 6780	1387	118	0.86
2200	6620 6845	1082	134	0.83
2300	6685 6835	784	132	0.94
2400	6730 6840	526	56	0.87
2500	6760 6740	262	102	0.54

Notes. The density is reported in stars per $25'' \times 25''$ bin; the fitted center is pixels in the master frame; A is the semimajor axis and B the semiminor axis, in WFC pixels; P.A. is the position angle of the major-axis, measured in degrees E from N. The last column represents the ratio of the minor to the major axis.

since we have at least four independent contours (based on their separation and the size of our bins), the center should be good to about 20 pixels, or $1''$.

4.2. The Pie-slice Method

The focus of the previous approach was to find the center of the cluster by identifying the centers of various isodensity contours of the stellar distribution. In this section, we describe how we divided the cluster into pie slices and determined the center by finding the location about which the stars are most symmetrically distributed.

The complication for this second approach is that the broad PSF halos of the few bright giants can cause a patchy incompleteness in the distribution of the faint stars, which can in turn cause us to find more stars on one side of the cluster than on another, and thus to misidentify the center. The contour-based approach in the previous section skirted this issue somewhat by focusing on the outer contours, where crowding is lower and the gradient is steeper; but the pie-slice approach will need to deal with incompleteness all the way into the center.

In order to measure an unbiased center, we had to construct a star list that is free of any incompleteness that would bias the center. This list must also contain enough stars to give us a statistically reliable result, so we could not simply use the few bright stars, which are essentially 100% complete. We clearly need to include the more plentiful faint stars, but including them requires taking careful account of incompleteness. Our AS tests from Section 3.5 provided one way to assess the incompleteness in the field. Unfortunately, it was not feasible to run enough AS tests to assess completeness on scales small enough to adequately sample the local region around each bright star. What we needed was a simple map of the field that could tell us how bright a star must be in order to be found in a particular place in the field. If we had such a map, we could then create a mask that is symmetric about any presumed center, so that the exclusion zones caused by the bright stars would be symmetric, and hence would not bias the center determination.

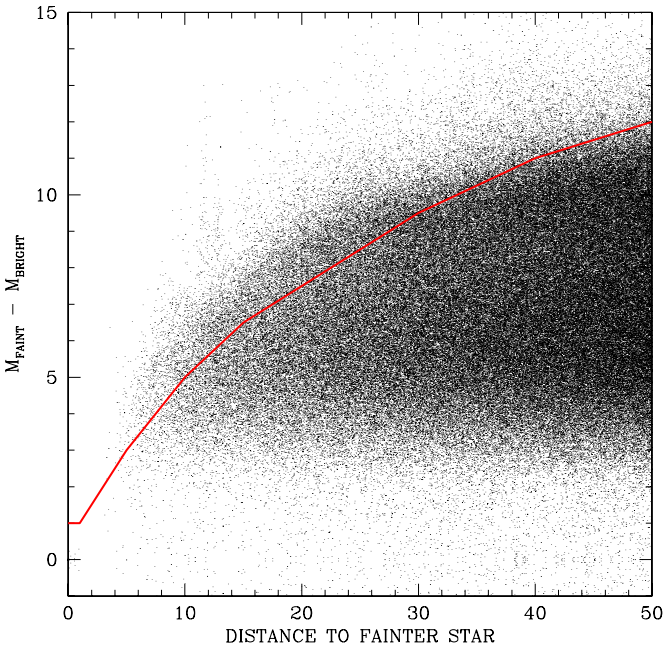

Figure 12. Distribution of found stars in the vicinity of brighter stars ($m_{F435W} < -16$). The solid line (red in the online version) indicates the faintest magnitude of star that could be definitively found at a given distance from a brighter star.
(A color version of this figure is available in the online journal.)

4.2.1. Completeness Mask

Our goal in constructing a mask was to determine, for a particular bright star, where in its vicinity a given faint star could be reliably found. To answer this question, we identified the bright stars with $m_{\rm F435W} < -16$ (about 10 × saturation) and looked at the distribution of their found neighbors as a function of distance from them. This distribution is shown in Figure 12. At a distance of 10 pixels, only stars that are within 5 mag of the bright star's flux can be found; fainter stars than this cannot be found reliably. Out to a distance of 20 pixels, stars up to 7.5 mag fainter than the bright star can be reliably found. This d versus Δm relationship is quantified by the red line drawn in the figure. A few stars above this line are found, but essentially, *all* the stars below this line are found.

Note that there are very few artifacts above this line; normally bumps in the PSF at regular distances and offsets are identified as stars by automated finding algorithms. We have almost no such artifacts in our lists because our initial finding procedure had a model of the PSF out to tens of pixels and the procedure was careful not to identify faint stars where appreciable PSF features are likely to be present (see Figure 3 of A08). If we had identified every bump in every image as a star, then there would be a large number of detections in a distinct pattern above the line. (Figure 1 of McLaughlin et al. 2006 shows what the unscreened PSF artifacts look like in this space.)

The red line in Figure 11 allows us to construct a zone around each bright star that tells us which stars stand out clearly at each distance. We brought the information from all the bright stars across the entire field together in order to construct an image that tells us how bright a star must be at each point in the field in order to be definitively found. The value of each pixel in this image tells us the magnitude of the faintest star that could be reliably found at each point. Figure 13 shows the F435W image of the central region of the cluster. The middle panel of the figure shows the finding mask constructed from these stars.

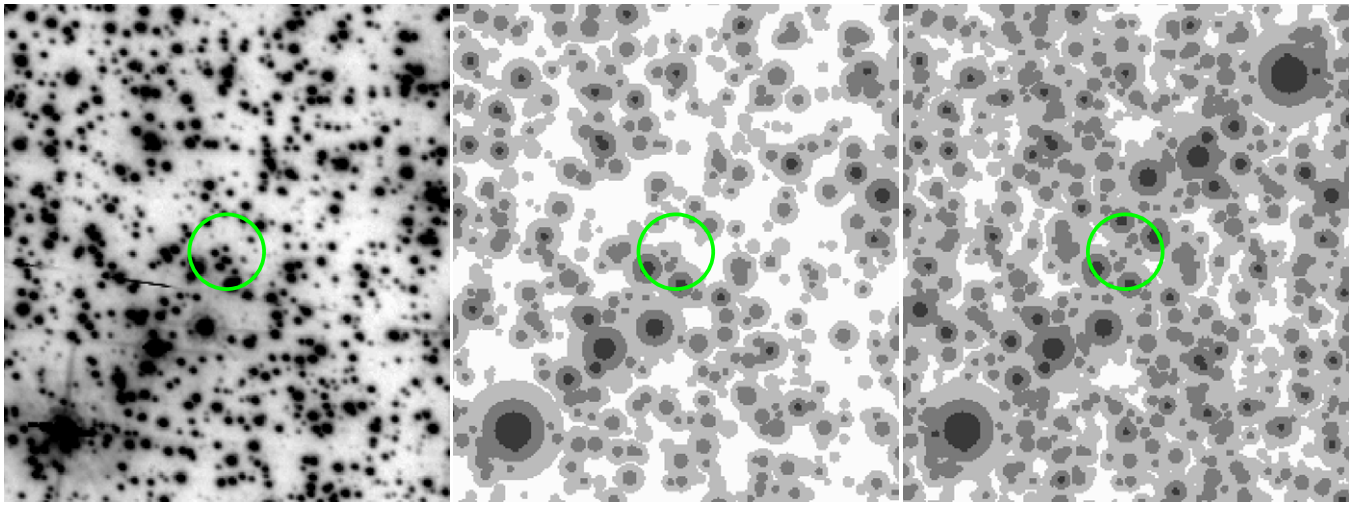

Figure 13. On the left, we show a $10'' \times 10''$ F435W image of the of central field. In the middle panel, we show the mask for the same region. The mask shown here has been gray-scaled to show the areas where stars of brightness -8, -10, and -12 can and cannot be found. The $m_{\rm F435W} \lesssim -8$ stars can be reliably found only in the white areas. The $m_{\rm F435W} \lesssim -12$ stars can be found everywhere except for the very darkest areas. The actual mask used for the analysis has much more gradation than is shown here. On the right, we show the mask after it has been symmetrized about a presumed center (very close to the actual center).
(A color version of this figure is available in the online journal.)

This mask essentially corresponds to an additional selection requirement: stars must have been identified by our automated procedure *and* they must also satisfy this location-based requirement. The goal of the mask is not to perfectly reflect our AS tests, but rather to provide an estimate of which stars could definitively be found at various points in the field. We validated this assumption using the AS tests: we verified that artificial stars were indeed recovered essentially everywhere the mask says they should be recovered.

One final note about the finding mask. There is a gap in the northwest part of our field (see Figure 1). Since no stars could be found where there was no coverage, we assigned the mask a value of -25 in this region. For reference, the brightest star in the field has an instrumental magnitude of -20.28 in F625W.

4.2.2. Symmetrization

The inferred mask made it possible to create star lists that have symmetric incompleteness properties with respect to any adopted center. With this tool in-hand, we next determined the best center using a pie-slice procedure similar to that used in McLaughlin et al. (2006). To do this, we assumed an array of trial centers. About each trial center, we divided the stars into pie slices centered upon that location and computed a statistic to compare the cumulative radial distributions of the stars in opposing pie slices. We finally identified the center as the place in the field that has the most similar radial distributions in the opposing pie slices.

Specifically, we decided to use eight pie slices, arrayed in cardinal and semi-cardinal directions (see Figure 14). We explored centers within the range of reference-frame coordinates [6400:7200,6400:7200], with a trial center every 20 pixels ($1''$) in each coordinate. In order to ensure that our star lists did not have any asymmetric biases, for each prospective center (I_c, J_c), we generated a list of stars by asking whether each star in the catalog would be found both at its own location in the mask (i_*, j_*), and at the location on the other side of the center $(I_c - [i_* - I_c], J_c - [j_* - J_c])$. If the star satisfied both criteria, it qualified for the center-determination list. The rightmost panel in Figure 13 shows what the mask looked like when symmetrized about a point near the ultimate center. A star that could not be found at one place in one slice would be excluded from the corresponding place in the opposing slice.

We next selected the stars that both satisfied this symmetrized-mask criterion and were brighter than $m_{\rm F435W} = -9$ within 4000 pixels radial distance ($200''$), and distributed them among the eight pie slices according to their azimuthal angle. We sorted the stars in each slice by distance from the adopted center, then for each of the four opposing pie-slice pairs we computed $\sum_{n=\min(N_1,N_2)} |r_1(n) - r_2(n)|$, which is the integrated difference between the radial distance r versus cumulative $N_{\rm encl}$ distribution functions for the opposing slices. This statistic was constructed for the four opposing pairs of slices at each trial center.

Figure 14 shows the result for our pie-slice analysis. The four pairs of opposing slices allow us to construct two independent estimates of the center, shown in the contours in the top plots. We fit a paraboloid to the central 9×9 points in the contour plot to arrive at the best-fit center for each panel. The plot in the upper-right panel shows the agreement between the two centers, and the two central contours. The plot on the bottom-right shows the contours constructed from all four pairs of opposing slices. The difference between the two center estimates is $2''$, indicating that our average center is probably good to about $1''$. In this determination of the center, we used about 235,000 stars. With a core radius of $150''$, we would expect the center to be accurate to about $150'' / \sqrt{235000}$ or about 0.3 arcsec; this is not a huge discrepancy if we consider that the cluster distribution is not Gaussian and the star lists used here did not extend out beyond two core radii.

We conducted the same procedure with a subset of our stars, using only those stars with $m_{\rm F435W} < -10$ and $m_{\rm F435W} < -11$, and found very similar results. Table 6 summarizes our findings. Overall, the centers determined by the different brightness cutoffs are consistent.

The center we found from the contour-based study in Section 4.1 was (6727,6810), which is in excellent agreement with the (6723,6811) location found here for $m_{\rm F435W} < -10$. In what follows we will adopt a center of (6725,6810) for the number density of Omega Cen, with an estimated error of $\sim 1''$ in each coordinate.

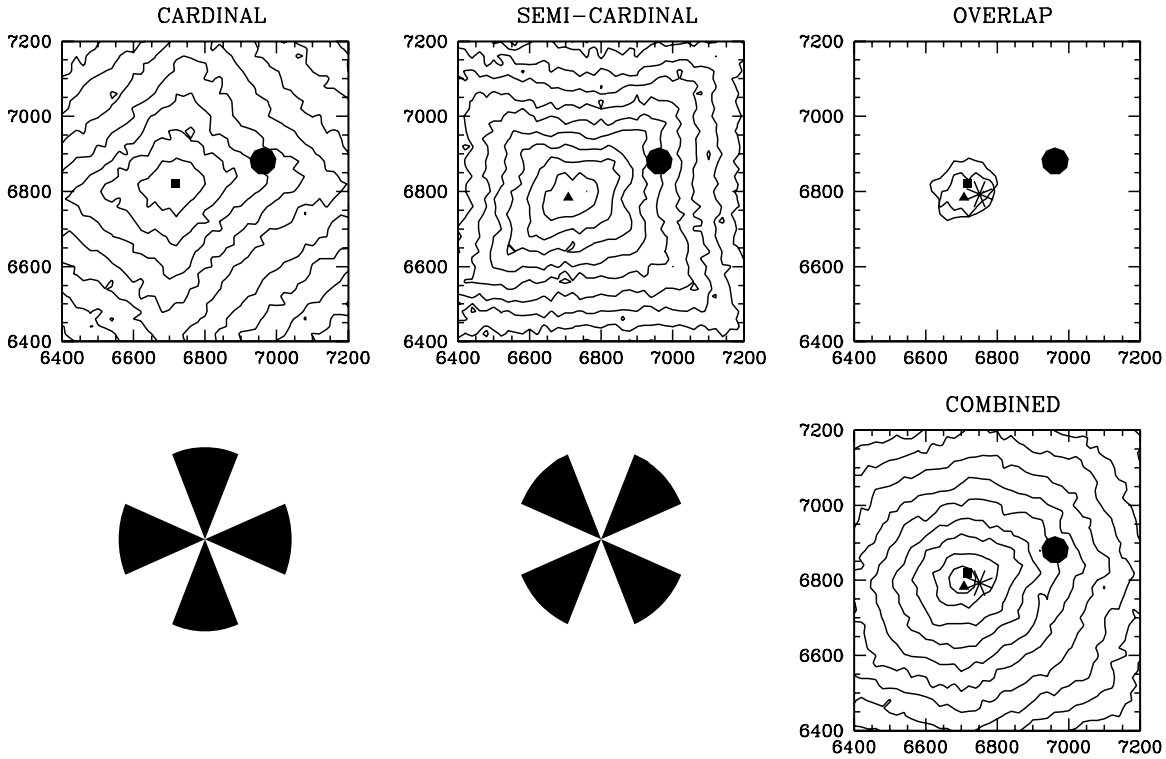

Figure 14. Two contour plots to the left show the goodness-of-center parameter for the pie slices shown below. The symbol at the center represents the paraboloid fit to the 9 × 9 points centered on each minimum. In the upper right, we compare the innermost contours and the fitted centers. In the lower right, we add the two goodness-of-fit metrics to get an overall best fit. The filled circle is the center from NGB08, and the six-pointed star is the center from the contour-based determination. The small square and triangle correspond to the center of the cardinal and semi-cardinal contours, respectively.

Table 6
Summary of Center Determinations Using the Pie-slice Method

Selection	Number	Cardinal	Semi-cardinal	Together
$B_{435} < -9$	235,000	(6718,6820)	(6718,6820)	(6703,6801)
$B_{435} < -10$	205,000	(6723,6837)	(6738,6784)	(6723,6811)
$B_{435} < -11$	150,000	(6736,6854)	(6759,6807)	(6747,6829)

Note. All positions are reported in our reference frame.

4.3. Kinematic Center from the Proper-motion Dispersion Field

An independent method to verify the results from the previous subsections is to find the kinematic center. In the present context, that means identification of the point of symmetry in the proper-motion velocity-dispersion field. Unlike the star-count analysis, the kinematic center determination has the advantage of being independent of any incompleteness corrections (so long as the kinematics of a star do not affect whether or not a star makes it into the catalog).

We took the full proper-motion catalog for the central field and binned the stars onto a grid of $1'' \times 1''$ pixels. The few stars believed to be outside the cluster (as indicated by Figure 8(d)) were excluded from the analysis. For each pixel we calculated the number of stars as well as the second proper-motion moment $(\mu_x^2 + \mu_y^2)$ summed over the stars. This yields two images, which we will call $N_0(x, y)$ and $N_2(x, y)$. These images are quite noisy, due to the relatively small number of stars per pixel. We therefore applied a two-dimensional top-hat smoothing kernel to each image to increase the S/N. This yields images $\hat{N}_0(x, y)$ and $\hat{N}_2(x, y)$. The implied smoothed image of the one-dimensional rms proper-motion $\sigma(x, y)$ is given by $[\hat{N}_2/(2\hat{N}_0)]^{1/2}(x, y)$. In practice, we found that a top-hat kernel radius of $25''$ yields adequate results.

The resulting rms proper-motion image $\sigma(x, y)$ is shown in Figure 15. There is a well-defined symmetric distribution around a broad central peak. The irregular outer boundary of the image represents the intersection of the two (approximately square) ACS/WFC fields for epochs 1 and 2, respectively. The cluster is not centered within this boundary, due to the particular details of the observational pointings. The closest boundary line is $\sim 70''$ south from the cluster center. In the kernel smoothing, we excluded all pixels that are outside the boundary region of the catalog. Nonetheless, properties of the map within $25''$ from the boundary may be somewhat affected by artifacts induced by the absence of data outside the boundary. To ensure that this would not bias the determination of the cluster center, we restricted our analysis of the map to radii $R \lesssim 45''$ from the cluster center.

We performed ellipse fits to the image to determine the symmetry point of the map. We adopted the average ellipse center for semimajor-axis lengths between $35''$ and $45''$ as our final estimate. The result lies at $(\Delta_x, \Delta_y) = (-1\farcs1, -2\farcs0)$ from the adopted star-count center. To determine the random errors in this center determination, we performed Monte Carlo tests. We created pseudo data sets by populating the same area of the sky covered by our catalog, with the same number of stars. The stars were drawn from the projected number-density profile derived in Paper II. Each star was assigned proper motions in the x- and y-directions by drawing random Gaussian deviates from distributions of dispersion σ. The value of σ was chosen to be a slowly decreasing function of radius, consistent with our measurements in Section 6 and Paper II. Proper-motion errors were added based on Gaussian deviates from randomly

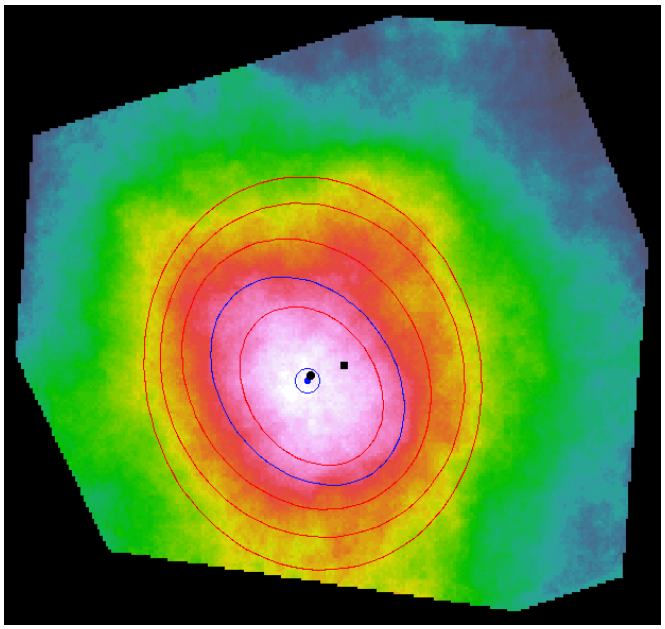

Figure 15. Velocity field of the one-dimensional proper-motion dispersion, smoothed with a 25″ radius top-hat kernel. The orientation of the image is as in Figure 11. The irregular outer border of the image is the intersection of the two (approximately square) ACS/WFC fields for epochs 1 and 2, respectively. At the chosen level of smoothing, the gradient in dispersion between the center and the edge of the field corresponds to ∼2 km s^{-1}. Ellipses are fits to the contours of the map, with semimajor-axis lengths of 30″–70″. The lower dot (blue) is the center of the ellipse (shown in blue) that has a semimajor-axis length of 40″. This is used as an estimate of the *HST* kinematic center, i.e., the symmetry point of the map. The small circle is the 68% confidence contour around the kinematic center, as determined from Monte Carlo simulations. The confidence contour shows that the kinematic center is consistent with the *HST* star-count center (upper dot, black). The center adopted by NGB08 (black square) is 12″ away, and is inconsistent with both of the *HST* centers.

selected error bars in the observed catalog. Each pseudo data set was analyzed in similar fashion as the real catalog. The Monte Carlo kinematic centers thus determined had an rms scatter of 2.″9 per coordinate around the input center, with no bias. The elongation of the $\sigma(x, y)$ contours in Figure 15 was found not to be statistically significant. Ellipticities as large as the observed value (at $R = 40''$) of ∼0.23 happened by chance in 14% of the Monte Carlo simulations.

To further ensure the robustness of the results, we also experimented with alternative approaches. These used percentiles of the proper-motion distribution (instead of the rms), different grid sizes, different smoothing kernels, or different kernel sizes. The results were always consistent with those quoted above. We also applied the method to the high-quality proper-motion subsample, instead of the full proper-motion catalog. This too yielded consistent results, albeit with larger uncertainties.[2] This is because the full catalog provides a larger sample size than the high-quality subset. Although the full catalog has somewhat larger proper-motion uncertainties, these uncertainties have essentially no impact on the analysis (although they are fully included in the simulations). They are always much smaller than the cluster dispersion. Therefore, the errors in the map of Figure 15 are determined primarily by the number of stars that contribute to each pixel ($\Delta\sigma \approx \sigma/\sqrt{2N}$), and not by the individual per-star proper-motion uncertainties. For the adopted kernel size, $N \approx 6000$ near the center. This yields random errors of ∼0.15 km s^{-1}, which is much smaller than the gradient in the dispersion map (in fact, the size of the kernel was purposely chosen to make this the case).

Our method is purposely designed to measure the symmetry point of the proper-motion map. One could use the peak of the map, but this quantity is much more affected by shot noise, due to the intrinsically low spatial gradients in the core of Omega Cen. Specifically, the peak of the proper-motion dispersion map in Figure 15 is at $(\Delta_x, \Delta_y) = (-6'', -7'')$ from the adopted star-count center. However, the Monte Carlo simulations show that the peak pixel, when used as an estimate of the cluster center, has an rms uncertainty of 6.″7 per coordinate. This uncertainty gets even larger if one chooses a smaller smoothing kernel size than the 25″ used here. So while the observed peak is statistically consistent with the symmetry point, it is a much more unreliable estimate of the true cluster center.

This makes an important point that underlies all our analyses: Omega Cen has such a large and (nearly) homogeneous core, that to determine its true center most accurately, one must locate the symmetry point of its large-scale distribution. Measures of possible small-scale peaks in density, star light, or kinematics, are much more susceptible to shot noise. While this does not make such estimates incorrect, they can only be interpreted if their uncertainties are rigorously quantified.

4.4. Kinematic Center from the Pie-slice Method

As an alternative approach to determination of the kinematic center, we also used a pie-slice method. For a given trial center, we adopt a polar grid with N azimuthal wedges (N chosen to be even) and M radial bins along each wedge. The radial bins are linearly spaced and have size S. The value of M is chosen so that $M \times S \approx 100''$, and the grid therefore encompasses most of our central-field catalog. For each bin, we use our full proper-motion catalog to calculate the proper-motion dispersion σ and its error $\Delta\sigma$ as in Section 4.3. For each pair of radially opposing bins, we calculate the quantity $(\sigma_1 - \sigma_2)^2/(\Delta\sigma_1^2 + \Delta\sigma_2^2)$, which measures the extent to which the dispersions in the two bins are statistically consistent with each other. When summed over all the opposing bins, this yields a χ^2 quantity. The number of degrees of freedom $N_{\rm DF}$ is normally $M \times N/2$. However, we exclude pairs that do not have a sufficient number of stars in each bin to yield a meaningful dispersion. Each pair thus excluded reduces $N_{\rm DF}$ by one. We map the quantity $\Delta\chi^2 \equiv \chi^2 - N_{\rm DF}$ on a grid of trial centers with 1″ spacing. We smooth the resulting map with a Gaussian with a 2″ dispersion (this smoothing is not required, but was found to reduce the uncertainties in the resulting kinematic center estimates by ∼15%). The trial center with the lowest $\Delta\chi^2$ is the position with respect to which the proper-motion dispersion field is most radially symmetric.

To minimize any dependence of the results on the somewhat arbitrary choices of N and M, we repeated this procedure for $N = 4, 6, 8, 10, 12, 14, 16$ and $S = 6, 9, 12, 15, 18, 21, 24$ arcsec. We summed the $\Delta\chi^2$ maps from all the 49 combination of N and S to obtain one grand-total $\Delta\chi^2$ map. The lowest $\Delta\chi^2$ in this map occurred at $(\Delta_x, \Delta_y) = (-0.''4, -1.''5)$ from the adopted star-count center. We used the same pseudo-data sets as in Section 4.3 to characterize the uncertainties in the result. Each pseudo data set was analyzed in similar fashion as the real catalog. The Monte Carlo results had an rms scatter of 1.″9 in x and 2.″4 in y. This measures the uncertainties in the inferred kinematic center. The Monte Carlo results were found to be slightly biased, and were centered on $(\Delta_x, \Delta_y) = (-0.''4, -0.''6)$. Since this bias can be calculated and corrected, it is does not

[2] Specific results were included in an earlier preprint version of this paper. These are now superseded by the analyses presented here.

affect the accuracy of the final result. The bias, and also the fact that the scatters differ in the two coordinate directions, are due to the specific geometry of our proper-motion data set.[3] Upon bias correction, the pie-slice estimate for the kinematic center is $(\Delta_x, \Delta_y) = (0\farcs0 \pm 1\farcs9, -0\farcs9 \pm 2\farcs4)$. We repeated the whole analysis also with only the high-quality observed proper-motion sample. This again yielded consistent results, but with somewhat larger uncertainties.

The kinematic center thus determined using pie slices is very consistent with the value derived from contour fits in Section 4.3. In fact, all methods that we have explored to determine the kinematic center yielded the same answer to within the uncertainties. The pie-slice method yields the lowest uncertainties, because it uses more of the large-radius information in the catalog (data points with $45'' \leqslant R \leqslant 100''$ are now included). We therefore use the pie-slice result as our final estimate for the kinematic center.

Our analysis provides the first time that the kinematic center of any GC has been accurately determined. The kinematic center of Omega Cen was found to be consistent with the star-count center. This is what is expected in an equilibrium system, and therefore should not come as a surprise. However, this is important since it provides an independent verification of the center position determined from the star-count analysis.

4.5. Comparison with the NGC08 Center and Other Literature Values

In Section 3.1, we used the 2MASS point-source catalog to tie our master reference frame to R.A. and decl. The center we identified in this frame corresponds to $(\alpha, \delta) =$ (13:26:47.24, −47:28:46.45), with an error of about an arcsecond in each direction.

We were unable to find any other centers for Omega Cen in the literature that had quoted errors. The most recent determination of the center was done by NGB08, who found the center to be at (13:26:46.04,−47:28.44.8). It turns out that this absolute position was measured in the drizzled ACS images, and contains some systematic error due to errors in the guide-star-catalog positions (Koekemoer et al. 2005). If we identify their center from the star field shown in their Figure 2 (which corresponds closely to the absolute coordinate they report from the WCS header of image `j6lp05weq_drz`), then their center corresponds to (6962,6881) in our master frame, or (13:26:46.08, −47:28:42.9) using the 2MASS astrometric reference frame, which is (+237, +71) pixels or 12.3 arcsec away from our center.

Figure 16 provides in finding-chart format the locations of our star-count and kinematic centers determined from our *HST* analysis, with the error estimates indicated, as well as the center and IFU fields used by NGB08. NGB08 do not estimate the error in their center, so it is hard to say that our centers are formally in disagreement. However, given that they felt their center was within their $5'' \times 5''$ IFU field, it seems safe to assume our centers are in significant disagreement. We explore this further in Section 5.3.

Harris (1996) reports (13:26.45.9, −47:28:37) for the center in his online catalog. van Leeuwen et al. (2000) found a center of (13:26:45.756, −47:28:42.780) using the positions of the giant stars brighter than $B = 16$. This center is adopted by van de Ven et al. (2006) and Castellani et al. (2007). The Harris and van Leeuwen centers are also indicated in Figure 16. They are closer to the NGB08 center than to the center positions inferred by us. We explore the differences between these ground-based centers and our *HST* center further in Section 4.7.

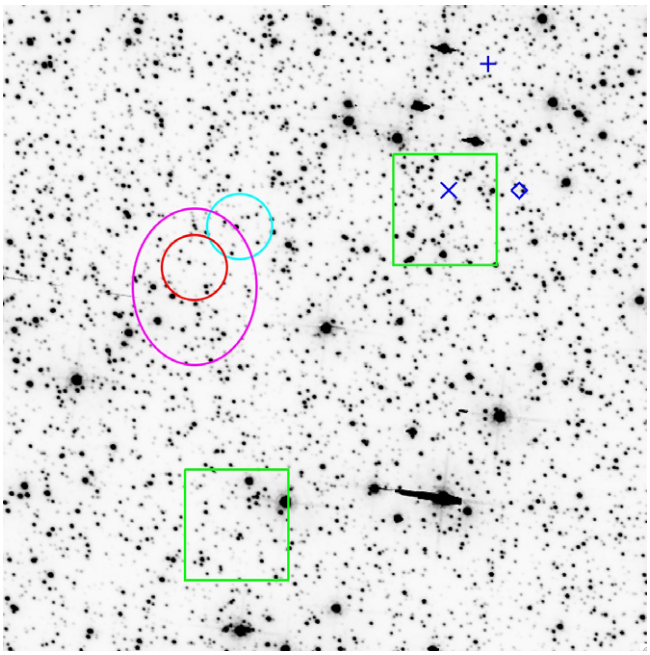

Figure 16. Central $30'' \times 30''$ of Omega Cen. Estimates of the cluster center from Harris (1996; plus), van Leeuwen et al. (2000; diamond), and NGB08 (cross) are shown in blue. None of these authors provided error estimates for their centers. The green boxes identify the two fields studied with IFU spectroscopy by NGB08, one of which was believed to include the cluster center. The circles/ellipses mark the cluster center positions determined in the present paper using various independent methods, namely, *HST* star counts (red; Section 4.2), *HST* proper motions (magenta; Section 4.4), and 2MASS unresolved light (cyan; Section 4.6). The sizes of the circles/ellipses indicate the 68.3% confidence regions of the estimates (note: for a two-dimensional circular Gaussian probability distribution, the circle that encloses 68.3% of the probability has a radius that equals 1.516 times the one-dimensional error bar). Our estimates are mutually consistent, and their uncertainties clearly rule out the previously reported values in the literature (see discussion in Sections 4.7 and 5.3).

Table 7
Various Centers

Reference	R.A.	Decl.	x	y	Δx	Δy	$\Delta r(''')$
This work	13:26:47.24	−47:28:46.45	6725	6810	...	...	...
NGB08	13:26:46.08	−47:28:42.9	6962	6881	+237	+71	12.3
Harris	13:26:45.9	−47:28:36.9	7011	6960	+286	+150	16.1
van Leeuwen	13:26:45.756	−47:28:42.78	7027	6883	+302	+73	15.5

Note. The NGB08 center has been corrected for *HST* guidestar errors.

In Table 7, we summarize the centers from the literature and compare them with the center determined here.

4.6. Center from 2MASS

Because of the disagreement between the center positions derived by us and those previously published in the literature, we sought non-*HST*-based data that could serve as an independent cross-check. The publicly available data from 2MASS proved suitable for this purpose. We downloaded a wide 2MASS image mosaic of the cluster using the NVO/ISRA mosaic service at http://hachi.ipac.caltech.edu:8080/montage/. The upper left panel of Figure 17 shows the *J*-band mosaic image. The pixel scale is 1 arcsec per pixel, and the field covers $14' \times 11'$.

[3] The bias can be avoided by using the method only with data closer to the center, instead of going out to 100″ where the azimuthal coverage becomes incomplete. However, that would produce larger uncertainties.

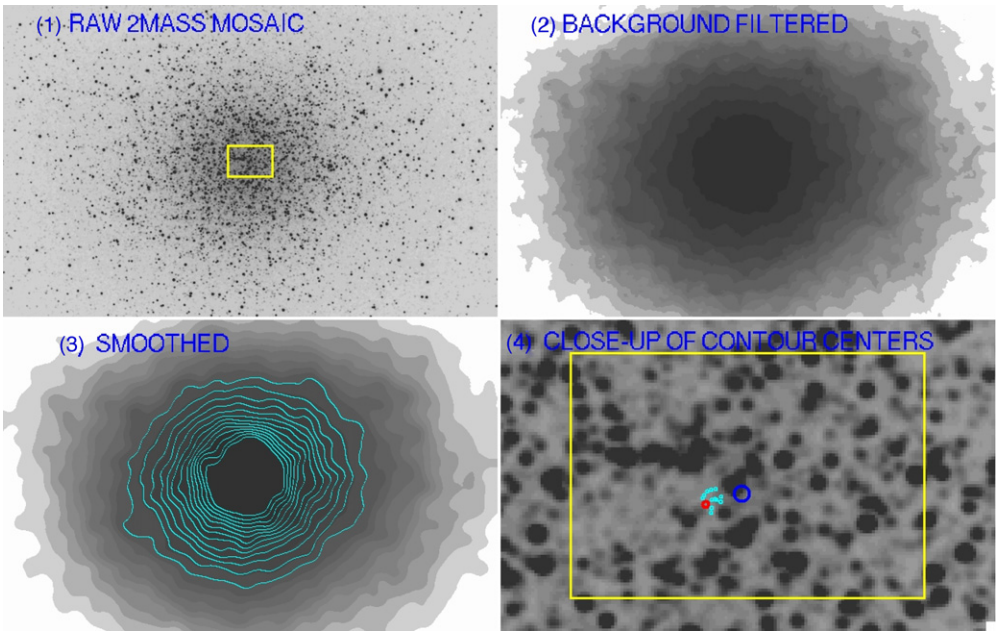

Figure 17. Upper left: 2MASS *J*-band mosaic centered on Omega Cen. Upper right: result of filtering the image to derive the underlying background (as described in the text). Lower left: result after additional top-hat smoothing, with contours drawn in. Lower right: close-up of the yellow-boxed region in the upper left panel. Locations of the contour centers are shown in cyan. The red circle is the *HST* star-count center derived here and adopted in our modeling; the 1″ radius of the circle corresponds to the one-dimensional error bar. The NGB08 center is shown in blue.

Since the 2MASS image was taken at near-IR wavelengths, it is extremely sensitive to the red-giant stars. In order to minimize the shot noise from bright stars on our analysis, we applied a "filter" to the image to isolate the underlying unresolved light. The filtering operation consisted of going through the mosaic image pixel by pixel, examining the surrounding pixels within a radius of 20 pixels (20″), and computing the tenth percentile of this neighbor distribution. The image on the top right of Figure 17 shows the result. It shows the general profile of the background light, but it is still patchy on account of the few bright stars.

We next smoothed this background-filtered image with a circular top-hat kernel that had a radius of 20 pixels, and arrived at the image in the lower left panel of Figure 17. This image is smoother and allows the derivation of a contour-based center. The blue lines are image contours between 2 core radii and 0.75 core radii, drawn at equal intervals of intensity. The adopted radial range is well suited for a determination of the center. It avoids the very central region, where the spatial gradient is too low to yield high accuracy. It also avoids, the outer region, where the results can be biased by uncertainties in the 2MASS sky-background subtraction process.

We fitted ellipses to the contours as in Section 4.1, and show the resulting centers overplotted in cyan in the bottom right panel of Figure 17. This panel shows a close-up of the yellow-boxed region in the upper left panel. The average of the centers lies at $(\Delta_x, \Delta_y) = (2\farcs1, 1\farcs9)$ from the adopted *HST* star-count center. The rms scatter in the ellipse centers is 2.″1 per coordinate. Given the kernel size for the percentile-filter and blurring operations, we estimate that about a third of the 12 contours between 2 core radii and 0.75 core radii are statistically independent. Therefore, the error in the mean position per coordinate is $\sim 2\farcs1/\sqrt{4} = 1\farcs0$. Given that the error in the *HST* center is also ∼1″, we find the centers determined from *HST* and 2MASS to be in acceptable statistical agreement. By contrast, the 2MASS position is 9.″8 from the NGB08 center, and even further from the Harris (1996) and van Leeuwen et al. (2000) centers. It is therefore inconsistent with those centers.

Use of unresolved light, especially in the near-IR, is more prone to possible systematic errors than our analyses based on *HST* star counts and kinematics. Therefore, we would not assign the 2MASS result the same level of confidence as our *HST* results, despite the similar random error. However, the 2MASS result is useful as a cross-check. The fact that it agrees with our *HST* results indicates there is no reason to suspect some fundamental problem with using either *HST* or ground-based data to determine the cluster center.

4.7. Understanding the Differences in Ground-based Centers

To understand how so many previous investigations could infer centers that differ so much from the centers found here, we need to address two separate questions: (1) why did previous authors who used ground-based data, such as Harris (1996) and van Leeuwen et al. (2000), derive centers that differ so significantly from that derived here from 2MASS? (2) Why did NGB08, who used some of the same *HST* data that we have, derive a center that differs so significantly from our star-count and kinematic-center results? We address the first question here. The second question is closely tied to the determination of cluster number-density profile from the *HST* data, and we therefore discuss it in Section 5.3 below.

We simulated a ground-based image by combining the *R*-band photometry from our (nearly complete) *HST* catalog with a broad, 3 arcsec FWHM PSF. This is shown in the upper-left panel of Figure 18. We also generated an image that represents the number counts for stars with S/N > 100 in the deep *HST* F625W exposures, distilled into the same 0.″5 pixels as the simulated image. These medium-brightness stars should not suffer much from incompleteness. The star-count image is shown in the upper right panel of Figure 18.

It is clear in the upper left panel that there are lines of bright stars in both dimensions that generate brightness enhancements

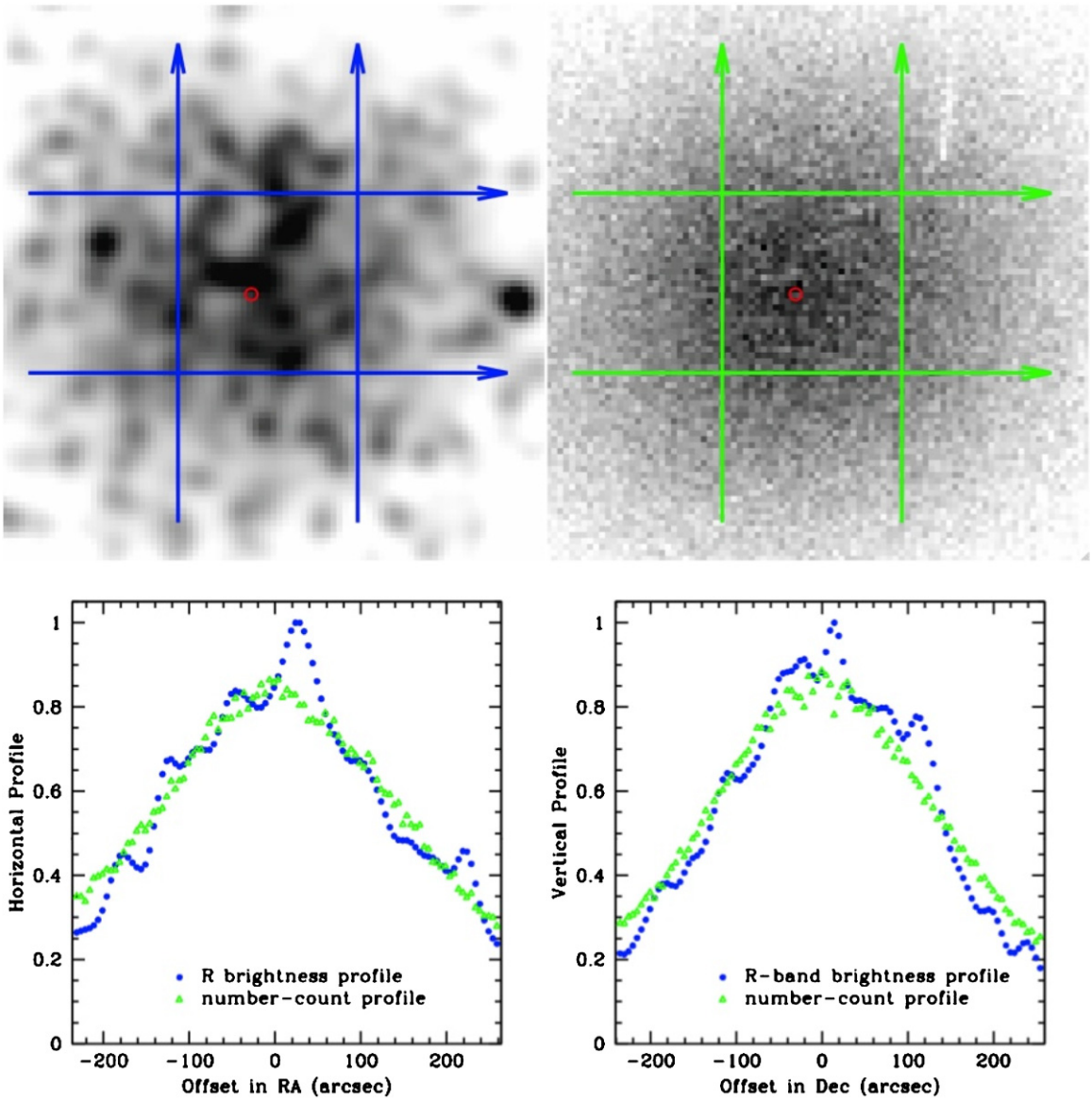

Figure 18. Upper left: simulated image with 3″ FWHM resolution of Omega Cen using our R catalog; upper right: number density of S/N > 100 stars from our catalog; lower left: horizontal profile of the two data sets; lower right: vertical profile of the two data sets. The arrows delimit the regions used in the creation of the profiles. The red circle is the *HST* star-count center derived here and adopted in our modeling; the 1″ radius of the circle corresponds to the one-dimensional error bar. The "traditional center" (Harris 1996) adopted in many studies of Omega Cen is at the center of the inner box. The offset shown on the horizontal axis of the bottom panels is measured with respect to the *HST* star-count center.

that cross at the rough location of the "traditional center." The latter is at the center of the box, roughly 15″ W and 10″ N of the *HST* center derived above, which is marked by the red circle. It is also clear that the visual centroid of the bright-star distribution is N and W of the *HST* center that we have identified. At the same time, the upper right panel shows that the bright, S/N > 100 sources are much more evenly distributed. They appear centered, as expected, around the previously derived *HST* center. Even by eye it is clearly evident that the S/N > 100 sources are *not* centered on the center of the box. The dark areas of the distribution extend more into the left and bottom parts of the panel than they do into the right and top parts.

We extracted horizontal and vertical profiles from each of these images. The lower left plot shows the horizontal profile across the 30″ tall swaths (between the horizontal arrows). The lower-right plot shows the same profile for the vertical direction. The blue points correspond to the simulated *R*-band image, and the green points to the number counts. It is clear that the traditional center corresponds to a location where there is a coincidental concentration of bright stars along both the *x*- and *y*-axis.

It is beyond the scope of this paper to determine how each previous determination of the center went wrong. In fact, many of the previous determinations did not provide a catalog or method description of sufficient detail to allow easy reexamination. Also, none of them provided an error estimate. Nevertheless, we have shown that a few bright stars are responsible for a light enhancement that is not coincident with the overall density peak of the more numerous, but fainter, stars. This light enhancement is close to the positions where previous authors estimated the cluster center to be. So it is likely that the methods previously used on ground-based data were disproportionately influenced by this light enhancement, and that this led to the historical misidentification of the center.

The analysis in Figure 18 does not imply that it is impossible to derive the cluster center from ground-based data. After all, we did manage to derive an accurate center from 2MASS data. However, what is clear from these analyses is that at a minimum one must adopt special methods to mitigate the shot noise from bright stars (e.g., through filtering as used in our 2MASS analysis).

5. SURFACE-DENSITY PROFILE

Our nearly complete catalog of stars, covering the inner two core radii of the cluster, allows us to calculate a definitive radial density profile for the inner part of the cluster. Note that the entire cluster cannot be described by a single radial profile, since the cluster contains stars of different masses at different stages of relaxation. If we consider only the profile of the evolved stars, then we will suffer small-number statistics, since only about 1% of the stars in our catalog are above the SGB. Our strategy here has been to measure the number-density profile for stars within a range of magnitudes. We note that number-density profiles do a much better job describing the star distribution than do surface-brightness profiles. A star at the tip of the red giant branch (RGB) is 100 times as bright as a star on the SGB, yet the two stars have essentially the same mass and should both be equally good tracers of the density distribution. Since the brighter stars are not better tracers of the star density, it makes sense that we should not give them more weight. Furthermore, since there are many times fewer evolved stars than SGB and MS stars, surface-brightness profiles suffer much more from shot noise than do number-density profiles.

5.1. Profile from the New HST Catalog

Our strategy in computing the number-density profile was straightforward. We divided the field into concentric annuli centered on the center derived in Section 4. Within each annulus, we determined the number of stars observed in each magnitude bin. We also determined the completeness for the magnitude bin for that annulus, based on the AS tests. We then constructed an average surface density within each annulus for each magnitude bin by dividing the number of found stars by the completeness.

Figure 19 shows the surface-density profile for three different brightness ranges, from the stars brighter than $m_{\rm F435W} = -13$ (just above the turnoff), to stars just below the turnoff at $m_{\rm F435W} \sim -11$, to stars well down the MS at $m_{\rm F435W} \sim -9$. It is hard to know exactly which profile we are most interested in. The profiles for the brightest stars tell us about the most massive luminous stars, but the fainter-star profiles have more stars, and therefore provide better constraints on the profile. All the profiles appear reasonably well fit by the single-mass King model we provide as a reference. Paper II fits the data with parameterized models, which will serve as the basis for our dynamical modeling.

There is no evidence of a sharp rise at the center in any of the profiles. Indeed, the central bin, which extends out to about $2''$ in radius, has fewer stars than the surrounding bins. Section 4 showed that our center is accurate to about $1''$, so the center should be well contained within our central bin. The completeness for all these bins is greater than 80%, even at the very center. Looking at the image in Figure 2, it is clear that there is not a significant increase in the vicinity of the center. Quantitative constraints on the central slope of the number-density profile will be presented in Paper II.

5.2. Comparison with the NGB08 Surface-brightness Profile

In their paper, NGB08 measured the surface-brightness profile, rather than the surface-density profile. They found that it rose with a power law with a logarithmic slope of -0.08 ± 0.03, which they deemed to be in significant disagreement with a flat core. This is at odds with our result, in that we found a different center and a relatively flat profile about it.

Since our data set is a super-set of the data they used, we decided to try to reconstruct their profile using our star catalog. In their work, NGB08 measured bi-weights of the background light distribution in the actual F435W image they used. We approximated their calculation by listing all the pixels within each of their annuli (centered on their center) and taking the 25th percentile of the points. This is plotted as the filled black points in panel (a) of Figure 20, and it agrees quite closely with the profile shown in Figure 1 of NGB08.

The NGB08 aim in measuring the surface brightness from the background was to be less sensitive to the bright giants and more sensitive to the numerous fainter stars. Unfortunately, most of the light in the background comes not from a large population of unresolved stars, but rather from the PSF halos of the bright stars. This can be seen from a simple examination of the luminosity function (LF). In an external galaxy where we cannot detect stars below the SGB, the LF is seen to increase steeply from the brightest stars to well below the detection limit, and as such there is a large reservoir of faint stars just below the detection limit. By contrast, in a GC such as Omega Cen, we resolve and count a large fraction of all the stars that are present. The stars that are not individually resolved contribute almost no light. In this sense, the analysis of unresolved light from *HST* data is different than for ground-based data. For example, the 2MASS images analyzed in Section 4.6 do not resolve individual stars on or below the SGB. So unlike the *HST* case, in the 2MASS images there is a large repository of unresolved stars that contribute a significant amount of light.

As a consequence of the fact that the LF is relatively flat below the detection limit, most of the background in the *HST* images comes from the bright-star halos rather than faint, undetected stars. Measuring the profile of the *HST* image background is therefore equivalent to measuring the profile from a blurred version of the bright stars. To demonstrate this, we simulated the field by taking the positions and brightnesses of all the stars in our catalog and using PSFs that go out to 100 pixels ($5''$), based on the encircled-energy curves in Sirianni et al. (2005). We performed the same 25th-percentile-based procedure on our simulated image, and arrived at the open dots, which trace the actual observations extremely well. There appears to be a constant offset of $\sim$100 electrons between the real and the simulated profiles, which can easily be accounted for by diffuse light scattered by even more than 100 pixels—the bright core of this cluster extends out to 3000 pixels (2.5 arcmin).

In panel (b), we show the number-density profile about the center adopted by NGB08. This profile does not increase as steeply and monotonically as the surface-brightness profile. To understand qualitatively how the surface-brightness profile was found to be more cuspy at the NGB08 center, panel (c) shows the placement of the NGB08 apertures in the field. Their central 50 pixel annulus happened to just contain a large number of turnoff-brightness stars. However, there is no evident central concentration of the more plentiful fainter stars, as a true cusp would suggest. The second annulus (from 50 to 100 pixels) contains a large number of bright RGB stars. The halos of these

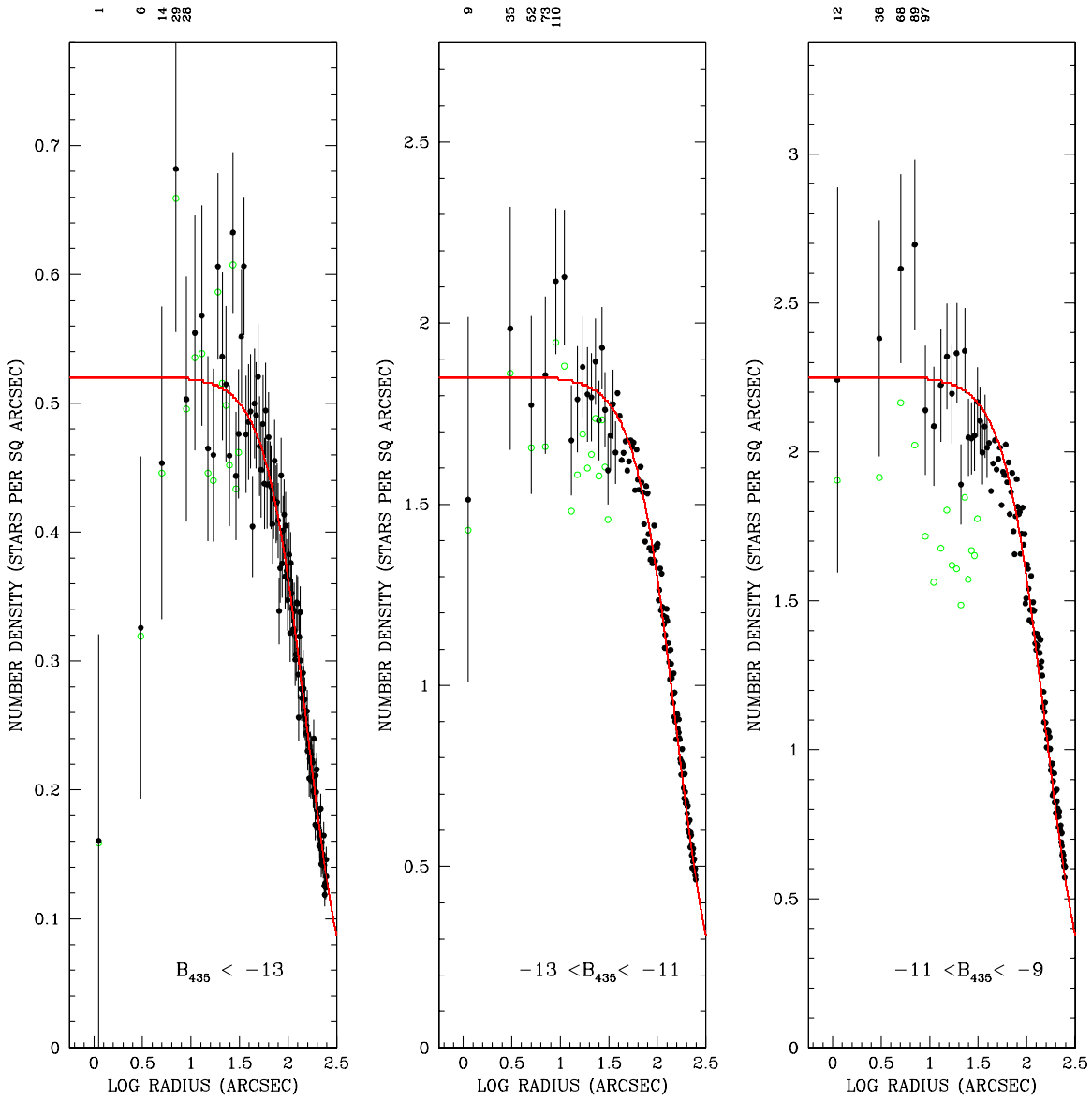

Figure 19. In each panel, we show the surface-density profile for stars in the labeled magnitude range (in stars per square arcsecond, with a linear scale). For reference, the bottom of the RGB is roughly at $m_{\rm F435W} = -13.5$. The filled circles have been corrected for completeness. The open circles (green in the online version) correspond to the density of stars actually observed (for clarity, we plot this only for the inner 50″). The error bars indicate the $\sqrt{N_{\rm obs}}$ errors. The radial bins are 2 arcsec wide; for the innermost five bins we note at the top $N_{\rm obs}$, the actual number of stars observed. The curve (red in the online version) corresponds to a single-mass King model with a core radius of 2.′5 and a tidal radius of 59′, shifted vertically to fit each profile. A more detailed quantitative analysis of model fits to the number-density profile is presented in Paper II.

(A color version of this figure is available in the online journal.)

encircling stars may help to explain why the background in the inner annulus was observed to be elevated.

5.3. Understanding the Differences in HST-based Centers

Both our study and the NGB08 study used *HST* data to determine the center of Omega Cen. It is therefore of interest to examine in more detail the differences between our results.

In Section 4, we have used the distribution of three quantities to determine the center of Omega Cen, namely, *HST* star counts, *HST* proper motions, and unresolved 2MASS background light. For each quantity, we used a contour-based method, and for the *HST*-derived quantities we also used a pie-slice method. The five different analyses all give the same answer to within the uncertainties of 1–2 arcsec. This effectively rules out the possibility that unexplored bias in any of the methods might have significantly affected the analysis. What the methods all have in common is that they identify the symmetry point of the cluster using data that extends significantly from the cluster center. This naturally uses the full size of the data set to reduce shot noise. The center thus identified is 12.″3 away from the NGB08 center. Hence, the NGB08 center is ruled out as the symmetry point of the cluster at 5σ–10σ confidence by each of three different quantities, analyzed with several different methods.

NGB08 used a pie-slice approach on *HST* star-count data to estimate the cluster center. The general method they used is described in Noyola & Gebhardt (2006), but few details are provided about the specific application to Omega Cen. Either way, there do appear to be two important differences compared to our analysis in Section 4.2. First, NGB08 applied no corrections for incompleteness. We believe that this is generally inadvisable when using star counts, although it is not clear whether this may have specifically affected their

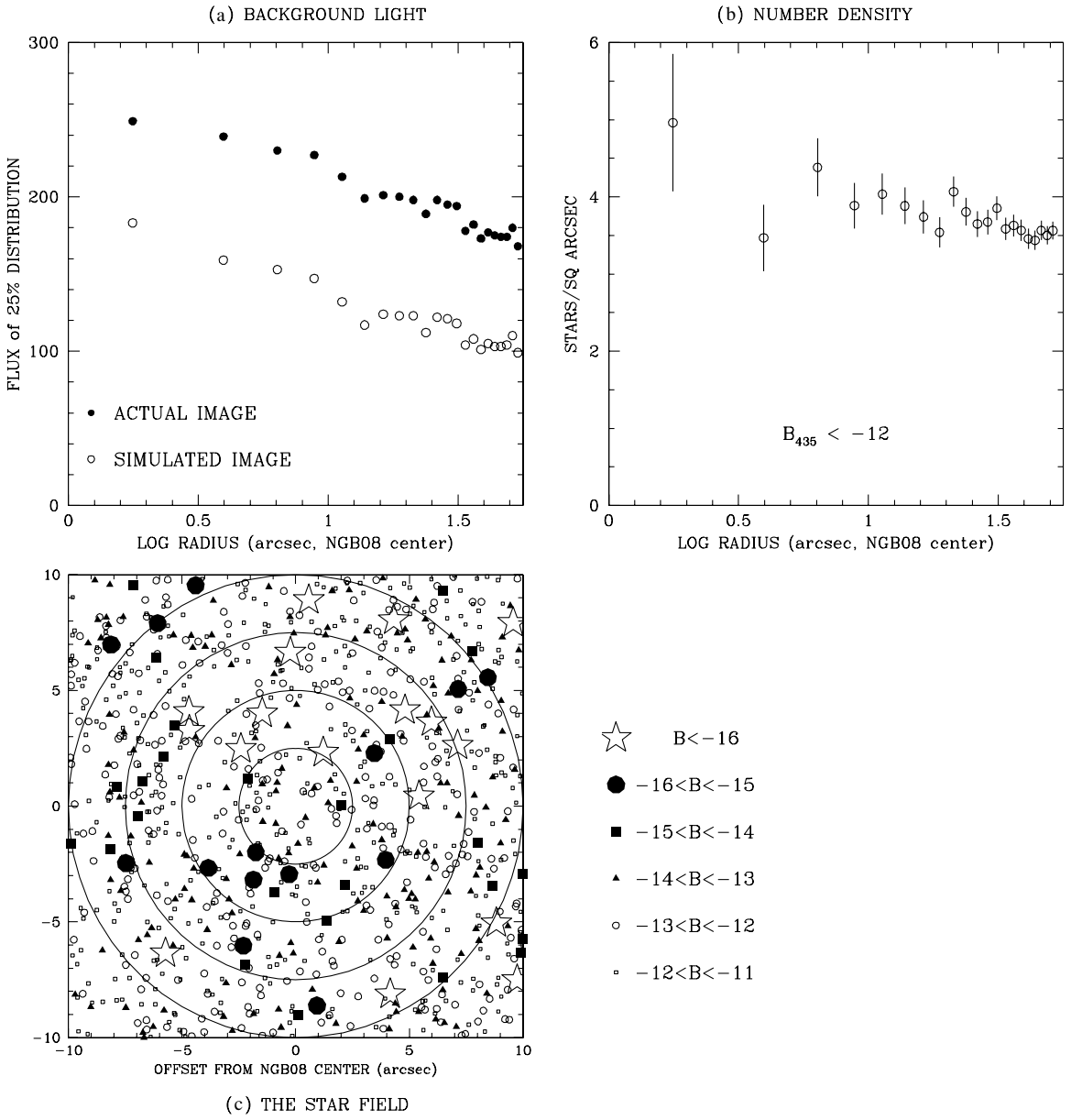

Figure 20. In panel (a), we show that if we use the NGB08 radial bins, and a percentile-based estimate of the background, we observe the same power-law radial trend they saw (filled black points). The open points represent the same procedure, but performed on a simulated image, as described in the text, which contains no faint unresolved stars. Panel (b) shows the number-density profile about their center. Panel (c) shows the catalog stars about the NGB08 center.

analysis. Second, the NGB08 center was measured from the same GO-9442 data set that we used, but from the text of their paper it appears that they used only the central pointing of the mosaic shown in Figure 1(a). This pointing was centered on the traditional center of Omega Cen, which could conceivably have introduced some bias. More importantly, the use of only the central pointing implies that their radial coverage went out to only 1.′5, which is significantly less than the core radius. As a result, their analysis may have been more sensitive to the peak of the density distribution rather than to the symmetry point. This appears supported by the fact that their method did in fact identify a density enhancement, as illustrated by Figure 20. This prompts the question whether there is any physical significance to this enhancement.

The central part of Omega Cen has a large core that is almost homogeneous. Within this core, spatial gradients in quantities of interest tend to very shallow. When only a finite number of stars are present or observed, one expects shot noise to dominate the small-spatial density distribution within the core. Some areas may be underdense while others may be overdense. This is in fact what we appear to be seeing. At the position that we have identified as the symmetry point of the cluster, the density appears somewhat underdense compared to its surroundings (see Figure 19). By contrast, at the position that NGB08 identified as the cluster center, the density appears somewhat overdense compared to its surroundings (see Figure 20). However, these features have the hallmarks of being noise-induced valleys and peaks. As such, their presence has no bearing on where the actual cluster center is.

The apparent underdensity at our center, as well as the apparent overdensity at the NGB08 center, appears most prominent when the shot noise is highest. In Figure 19(a), this is because the number of stars in the magnitude range $B_{435} < -13$ is low. In Figure 20(a), it is because of the use of unresolved

light (which emphasizes the shot noise from the brightest stars, which are small in number). By contrast, in Figures 19(b) and (c), and in Figure 20(b) the respective under- and overdensities are less prominent. Moreover, the error bars are such that the profiles are consistent with being flat to within the uncertainties. Specifically, the rise in the number density within 10″ from the NGB08 center (Figure 20(b)) is not statistically significant, and consistent with being a statistical fluctuation. The error bar on the central point is ∼20%, and the point just outside the center is lower than the average within the inner 10″.

Even a simple visual inspection of Figure 16 shows the core of Omega Cen is sparse and homogeneous enough to make identification of the center from local density enhancements either difficult or impossible. Instead, one should adopt a technique that focuses on the symmetry point of the larger-scale distribution. The data used for such an analysis must extend far enough out to cover and use the region where the density, brightness, and stellar motions start dropping significantly. From such analyses, we have found that the NGB08 center is definitely not the symmetry point of the cluster. Also, any light or density enhancement/cusp that may exist near the NGB08 center appears consistent with a statistical fluctuation in an otherwise (nearly) homogeneous core. On top of this, we show in Section 6.2 below that the proper motions near the NGB08 center do not in any way indicate that this position is special compared to its surroundings. We therefore conclude that the position identified by NGB08 is not the cluster center.

6. ANALYZING THE PROPER MOTIONS

The best way to constrain the presence of an IMBH in a cluster is to observe its effect on the motions of stars. NGB08 used an IFU on Gemini to measure the dispersion in the radial velocities of the unresolved light, and inferred a distinct rise in the velocity dispersion at their center, as compared with a field that was 14″ away (see geometry in Figure 16). We have demonstrated that the center they used is likely 12″ off from the true center. Nonetheless, if their velocity measurements are accurate, then they still imply an interesting kinematical feature within the core. To test this, we will examine the proper motions about their center and about the center we derived.

6.1. Proper Motions in the Central 10 arcsec

In Figure 21, we plot the total motions μ_D for the high-quality sample of stars (i.e., those flagged "good") in the central 10 arcsec as a function of distance from the cluster center. The total two-dimensional motions and errors are defined here as

$$\mu_D = \sqrt{\mu_x^2 + \mu_y^2}, \qquad \sigma_{\mu_D} = \sqrt{\sigma_{\mu_x}^2 + \sigma_{\mu_y}^2}. \qquad (1)$$

The radial axis is scaled as r^2 so that we will get a roughly even distribution of stars across the graph. The vertical lines divide the sample into groups of 100 stars. No star in the inner 10″ is moving faster than 3 mas yr^{-1}.

This plot shows that the distribution of motions at the very center (leftmost bin) looks very similar to that in the last bin at ∼10″. There are no more high-velocity stars at the very center than elsewhere in the distribution, contrary to what we would expect if an IMBH were present (Drukier & Bailyn 2003). The bottom panel examines the percentiles of the bin-by-bin distributions. In addition to seeing no particularly fast-moving stars at the center, we also see no indication of a rise in the dispersion at the center. Consistent with our cursory examination above, the percentiles in the central bin at ∼2 arcsec are indistinguishable from those in the outermost bin at 10 arcsec.

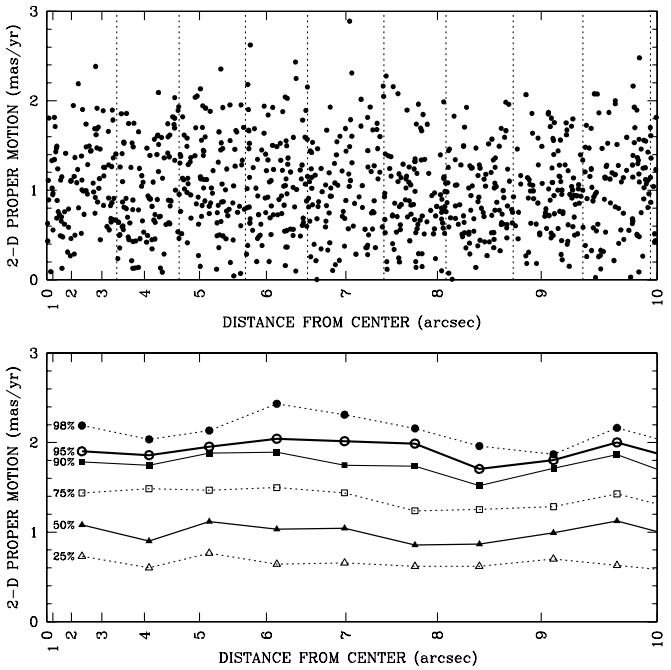

Figure 21. Top: the total proper motion $\mu_D = \sqrt{\mu_x^2 + \mu_y^2}$ for each star plotted as a function of distance from the center. Bottom: the percentiles of the distribution for the 100-star bins indicated in the top panel.

Figure 21 indicates that the proper motions of Omega Cen do not show an obvious kinematical signature of an IMBH. By contrast, a sufficiently massive IMBH would have induced increasing velocities toward the center with rms $\sigma \propto R^{-1/2}$. The question of what exact IMBH mass would be required to produce an observable signature is discussed in detail in Paper II. One important issue when addressing this question is that many of the stars in the centermost parts of the field are not truly close to the center but are merely projected there from somewhere between ∼ ±1 core radius along the line of sight. For example, for a projected aperture of 3″ radius around the center, only between 1.3% and 5.8% of observed stars reside within 3″ from the center in three dimensions. These numbers were calculated from number-density distribution models derived in Paper II (the "core" and "cusp" models, respectively). Only 43 stars in the high-quality subset of our proper-motion catalog reside within 3″ from the projected center. Hence, for an IMBH mass that produces a sphere of influence of order 3″, at most a handful of fast-moving stars would have been expected (see the quantitative analysis in Section 6.7 of Paper II). The bigger the IMBH mass, the more fast-moving stars would have been expected.

6.2. Comparison with the NGB08 Kinematics

The analysis in the previous section examined the motions in the central region out to 10 arcsec from our center, but it did not include the central field studied in NGB08. In Figure 22, we study the distribution of proper motions in the near vicinity of our center and the NGB08 center, in the context of the stars in the wider central region. The top row of plots shows the proper motions for the stars in the inner 15″; the middle and bottom rows show the same quantities for the stars within 3″ of our center and the NGC08 centers, respectively. There are 1200

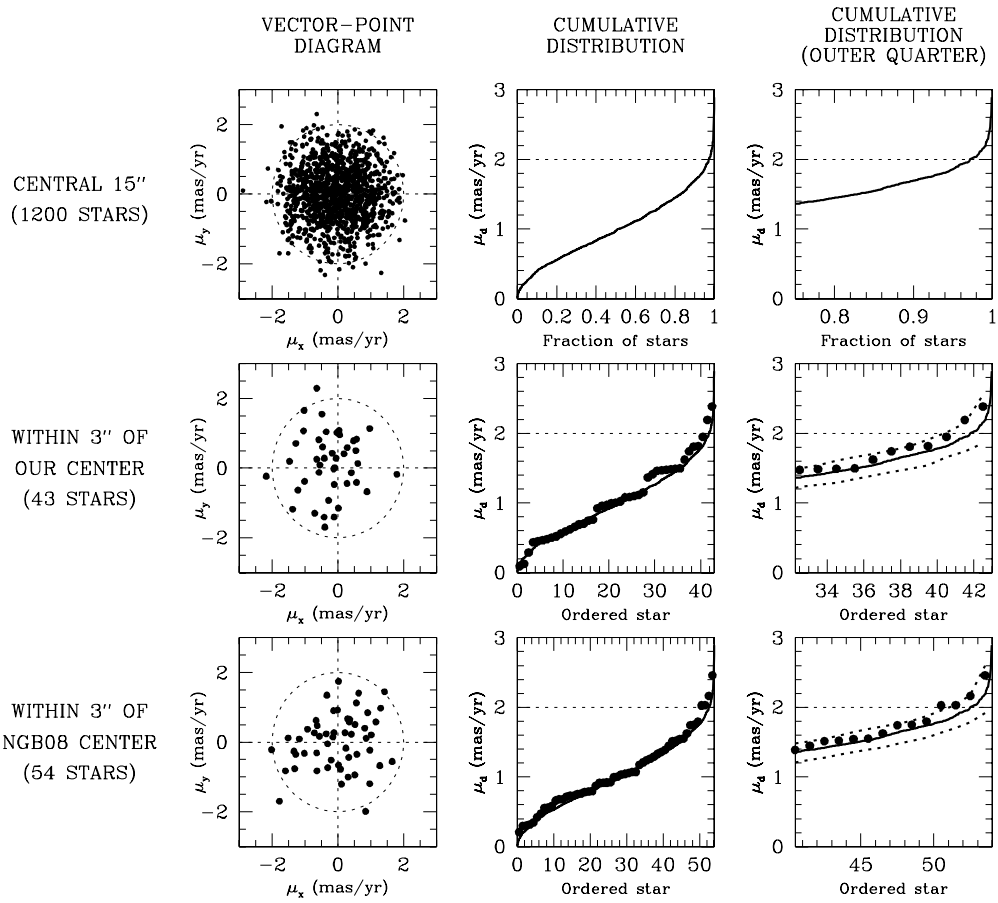

Figure 22. Comparison of the proper-motion distribution within the inner 15″ (top row of panels) and the distribution within 3″ of the two centers (bottom rows). The left panels show a vector-point diagram, the middle panels show the cumulative distribution of the two dimensional proper motions μ_D, and the right panels show the outer 25% of the cumulative distribution. The dotted lines in the bottom right plot indicate the 80% confidence region under the assumption that the underlying velocity distribution is the same as for the $R \lesssim 15''$ region in the top panel. The observations fall within the bands, indicating that there are no statistically significant differences between the distributions.

stars in the wider central region, 43 stars near our center, and 54 stars near the NGB08 center. We include here only stars from the high-quality proper-motion subset.

For each row, the leftmost panels show the proper-motion distribution as a vector-point diagram, and the right panels show the cumulative distributions. For the bottom two rows, we compare the cumulative distribution for the given small region against the cumulative distribution for the central region as a whole. The dotted lines in the right plots show the result of 1000 Monte Carlo tests based on the distribution function from the upper panel and the observed number of stars in the lower two panels. The dotted lines indicate the 80% confidence region under the assumption that the velocity distributions are the same.

We find that the motions of stars about our center and the NGB08 center are well described by the same distribution function that describes the stars within the inner 15″ of the cluster. Therefore, our proper motions do not confirm the velocity gradient reported by NGB08 in line-of-sight velocities, independent of the adopted center.

To compare our kinematics more directly to those of NGB08, we also studied the proper motions of stars in exactly the same two 5″ × 5″ fields that they studied (see Figure 16). In our high-quality proper-motion sample, there are 51 and 35 stars in their "central" and "off-center" fields, respectively. Each star has two orthogonal velocity components, so the number of data points available to estimate the one-dimensional velocity dispersion σ_{1D} is twice the number of stars. Using the methods described in Paper II, we find that $\sigma_{1\text{-}D} = 0.833 \pm 0.059$ mas yr^{-1} and 0.835 ± 0.071 mas yr^{-1}, for the central and off-center fields, respectively. For a canonical Omega Cen distance $D = 4.8$ kpc (van de Ven et al. 2006), these results translate to 18.9 ± 1.3 km s^{-1} and 19.0 ± 1.6 km s^{-1}, respectively. The similarity between these dispersions is consistent with the fact that we have determined both to be at roughly the same distance $R = 12''$ from the center (see Figure 16). These proper-motion dispersions are consistent with the values we measure throughout the rest of the central ∼15″ region of Omega Cen (see Paper II). NGB08 determined line-of-sight velocity dispersions $\sigma_{\rm los} = 23.0 \pm 2.0$ km s^{-1} and $\sigma_{\rm los} = 18.6 \pm 1.6$ km s^{-1} for these fields, respectively. Whereas our results agree with their measurement for the off-center field, our proper motions do not confirm the NGB08 result that the velocities in the central field are higher.

6.3. Radial Proper-motion Profile

Figure 23 shows the proper-motion distribution for the entire central data set, defined by the overlap region between the GO-9442 and GO-10775 data sets (see Figure 1), focusing on the percentiles of the distribution function (as marked on the plot). The plot on the left is more finely sampled and goes out to a radius of 50 arcsec. The plot on the right distills the stars into 2000-star bins and goes out to the corners of the central field, at 120″. The radial axis is once again scaled by r^2, so that we

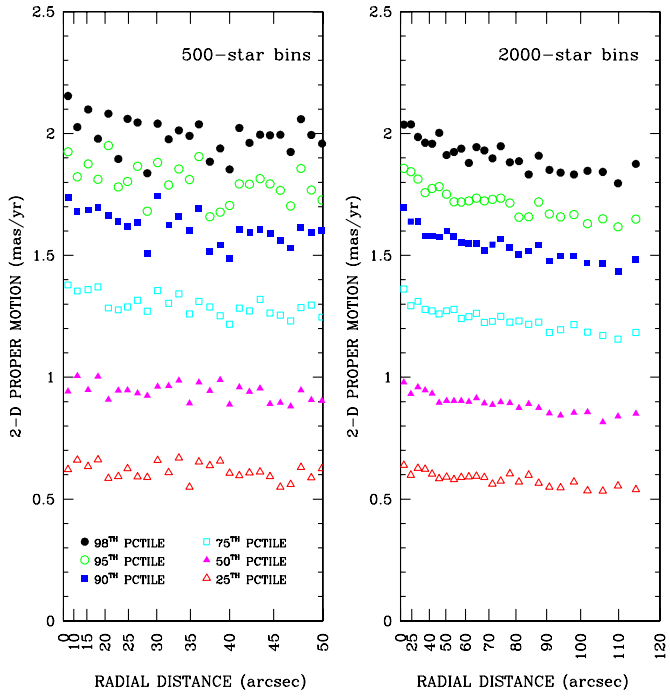

Figure 23. Left: similar to the bottom of Figure 21, but covering a larger radial extent. We take 500 stars at a time, and determine the percentiles of the proper-motion distribution, which we plot as a function of the median radius in the group. Right: same, for 2000-star bins, out to the edge of the inner data set. In a two-dimensional distribution, 50% of the points should be within 1.177 times the one-dimensional sigma ($\sigma_{1\text{-}D}$), and 75% should be within 1.665 $\sigma_{1\text{-}D}$.

(A color version of this figure is available in the online journal.)

will get equal number of bins with radius (where there is full azimuthal coverage).

While there is a distinct rise of about 10% in the PM dispersion from 80″ into the center, the left plot shows that there is very little increase within the inner 30″. This is as true for the wings of the distribution function (the black symbols) as it is for the core (the cyan symbols).

In Paper II, we will present a detailed analysis of the proper motions as a function of radius, including a determination of the velocity-dispersion and velocity-anisotropy profiles, comparison to literature data, calculation of higher-order Gauss–Hermite moments, a comparison between the proper motions in our central and major-axis fields, and a comparison between major-axis and minor-axis proper motions. Dynamical models will be fit to the data to constrain the possible presence and mass of any IMBH.

7. EXAMINING THE PROPER MOTIONS BY POPULATION

The primary motivation for the construction of a proper-motion catalog was to enable us to evaluate the likelihood of an IMBH at the cluster center (which we will further discuss in Paper II). However, this rich data set also can tell us much about the dynamical state of the cluster. In this section, we will do a cursory analysis of the data to examine the motions of stars with different masses and stars in different populations.

7.1. Equipartition

It is well known that Omega Cen has not had enough time for complete dynamical relaxation. Harris (1996) reports its half-mass relaxation time as 10^{10} yr. Anderson (2002) examined the LF at the cluster center and at a removed radius and found that the cluster does not demonstrate as much mass segregation as one would expect for a multi-mass King model in energy equipartition. To complicate the matter, Omega Cen has multiple populations of stars, and these populations exhibit spatial gradients and could have different mass functions. The present data set allows us to study the dynamics of the stars at a single location in the cluster (the center), thus avoiding the ambiguity introduced by comparison of populations at different radii.

In Figure 24, we show the distribution of the proper motions and proper-motion errors as a function of F435W magnitude. For this analysis, we used the full PM catalog from the central field, not just the high-quality subset, since we wanted to examine the motions of the faint stars. The CMD on the left highlights the stars that we selected for this study of the MS. The middle panel shows the distribution of PM errors for the stars that lie within the curves in the left panel. We selected for further analysis the stars that follow the general trend of PM error with magnitude in the middle panel, and show the motions for these stars on the right. Both x and y motions are shown in the same plot. Within each half-magnitude bin, we found the error-corrected one-dimensional rms, given the observed motions and errors for the stars in the bin. We report the rms on the right-hand side of the plot. The proper-motion dispersion clearly increases as we go down the MS. The rms motions discussed here, as well as other kinematical quantities discussed in the remainder of the paper, were determined using the maximum-likelihood methodology described in Appendix A of Paper II.

In order to interpret this velocity variation in terms of mass, we fit the CMD with an isochrone in the left panel of Figure 25, finding a reasonable fit to the upper population with a 12.5 Gyr isochrone from Pietrinferni et al. (2006) with alpha-enhancement, [Fe/H] $= -1.6$ and $Y = 0.24$. This isochrone allows us to associate a mass with each F435W magnitude. The masses for our magnitude bins are shown in panel (b). Finally, in panel (c) we show (solid points) the run of error-corrected rms proper motion with mass. If the cluster is in energy equipartition, we would expect the observed points to follow the upper curve, where velocity is proportional to $1/\sqrt{M}$. We see that the velocity does rise with decreasing mass, but not as rapidly as equipartition would predict. These results are consistent with the core being in the process of establishing equipartition, but only being about half-way there. Of course, it is well known that Omega Cen cannot be represented by a single isochrone. Combined with uncertainties in the exact distance, age, and metallicity, this causes small uncertainties in the absolute calibration of the mass for a given luminosity. However, this does not affect the conclusions about equipartition, which depend only on relative masses.

We have repeated the central-field equipartition analysis also for the adjacent major-axis field. The median radius for stars in the central-field catalog is 75″, whereas it is 218″ for the major-axis field catalog. As a result of this difference in distance from the cluster center, we find the rms proper motion to be higher by a factor of 1.22 in the central field than in the major-axis field. However, Figure 25(c) shows that the dependence of rms proper motion on stellar mass is the same in both fields (open points indicate the error-corrected rms proper-motion measurements for the major-axis field after renormalization by a factor 1.22). Therefore, we detect no significant difference in the amount of equipartition between approximately 0.5 and 1.5 core radii. In principle, one might have expected less equipartition at the larger

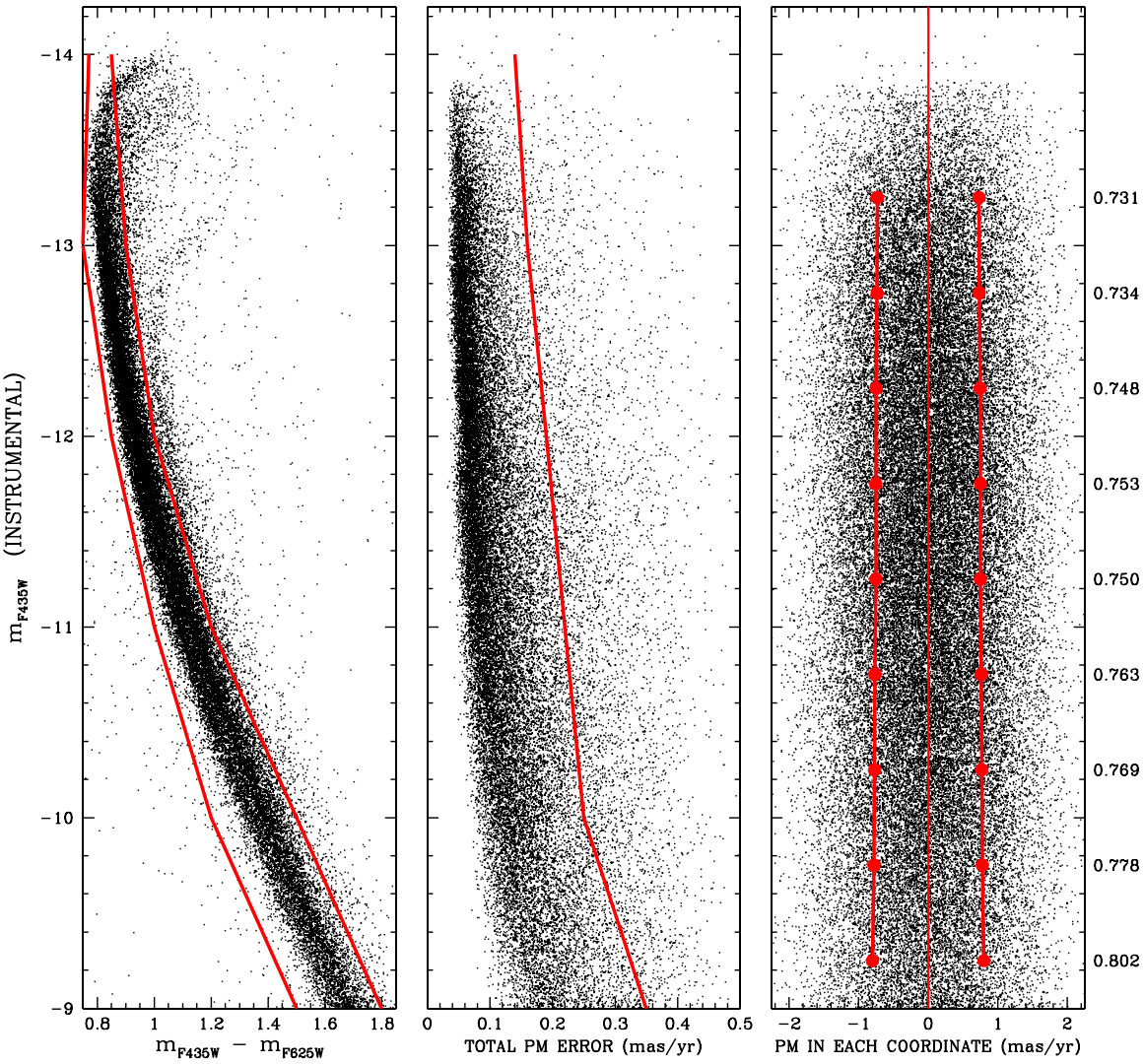

Figure 24. Left: CMD showing stars selected for main-sequence study (those within the drawn-in lines). Middle: the two-dimensional proper-motion errors σ_{μ_D} for stars as a function of instrumental F435W magnitude. Stars left of the drawn-in curve were used in the analysis. Right: the x and y proper motions for the selected stars plotted together. The curves indicate the rms as determined from a maximum-likelihood analysis that took into account the measured errors. The single-component rms for each half-magnitude bin is reported on the right.

(A color version of this figure is available in the online journal.)

radius, given that the two-body relaxation time increases with radius in Omega Cen (see Figure 21 of van de Ven et al. 2006). On the other hand, the radial range that we can probe is not large. Also, cluster rotation becomes a significant factor in the outer field, and this is not probed by our analysis (as discussed in Section 3.6.4). Detailed evolutionary models would therefore be required for quantitative interpretation of these results, which is outside of the scope of the present study.

In Paper II, we will compare the observed dispersions of line-of-sight velocities and proper motions in Omega Cen. The former are measured in km s^{-1}, while the latter are measured in mas yr^{-1}. With the aid of dynamical models, this provides a means of determining the cluster distance. However, mass segregation provides an added complication in such an analysis. The stars for which we have proper motions are slightly less massive than the stars for which we have radial velocities (almost all are giant stars). So even in the idealized case of an isotropic system, one would not expect to measure transverse and line-of-sight velocity dispersions that are the same in km s^{-1}. Figure 24 allows us to determine the size of this effect and correct for it, as discussed in Paper II.

7.2. Bulk Motion of the Metal-rich Population

Pancino et al. (2000) observed the RGB of Omega Cen from the ground in *B* and *I* and found evidence for three sub-populations: a metal-poor population (RGB-MP), an intermediate-metallicity population (RGB-MInt), and a metal-rich population (RGB-a), which comprises 5% of the RGB stars. Ferraro et al. (2002) then cross-identified these "RGB-a" stars in the proper-motion catalog of van Leeuwen et al. (2000) and found that they appeared to be moving at about 1 mas yr^{-1} relative to the rest of the cluster. They conjectured that this could represent a background cluster that may be in the process of merging with Omega Cen. This interpretation was disputed by Platais et al. (2003), who contended that it was likely to be a consequence of an uncorrected color–magnitude term in the plate equation. Recently, Bellini et al. (2009a) have constructed proper motions for stars in the outer regions of the cluster from ground-based CCD data spanning four years and determined that the RGB-a stars do in fact share the bulk motion of the cluster. We will use our *HST*-measured proper motions and population identifications to provide an additional determination of whether

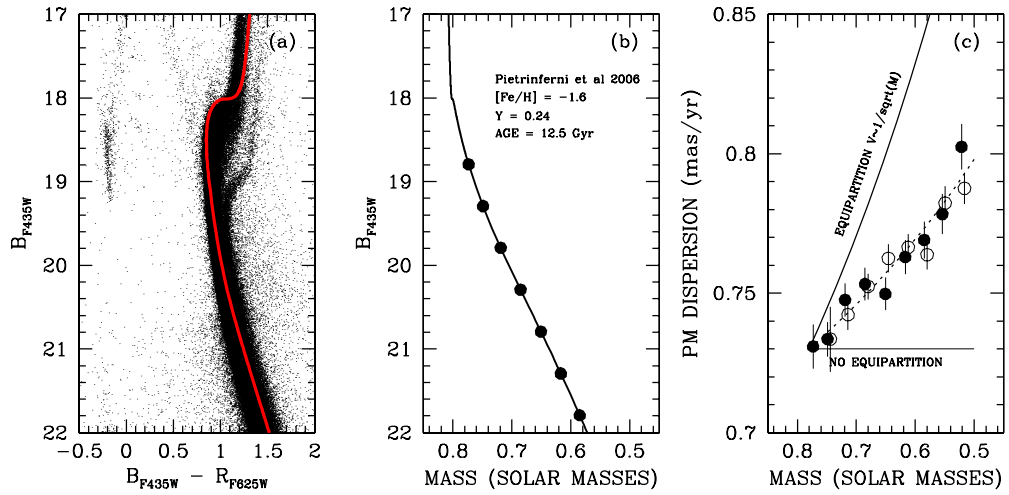

Figure 25. Left: the fit of our CMD with the [Fe/H] = −1.6 and $Y = 0.24$ isochrone from Pietrinferni et al. (2006). Middle: the mass–luminosity relation for the isochrone, with symbols at the locations of our luminosity-function bins. Right: the observed error-corrected one-dimensional proper-motion dispersion as a function of mass. The lines are drawn for comparison to indicate the trend that would be expected for complete equipartition $\sigma \propto M^{-0.5}$ and for no equipartition at all. The dotted line shows the intermediate case of $\sigma \propto M^{-0.2}$. Solid points show measurements for the central field; open points show measurements for the adjacent major-axis field, renormalized upward by a factor 1.22.

(A color version of this figure is available in the online journal.)

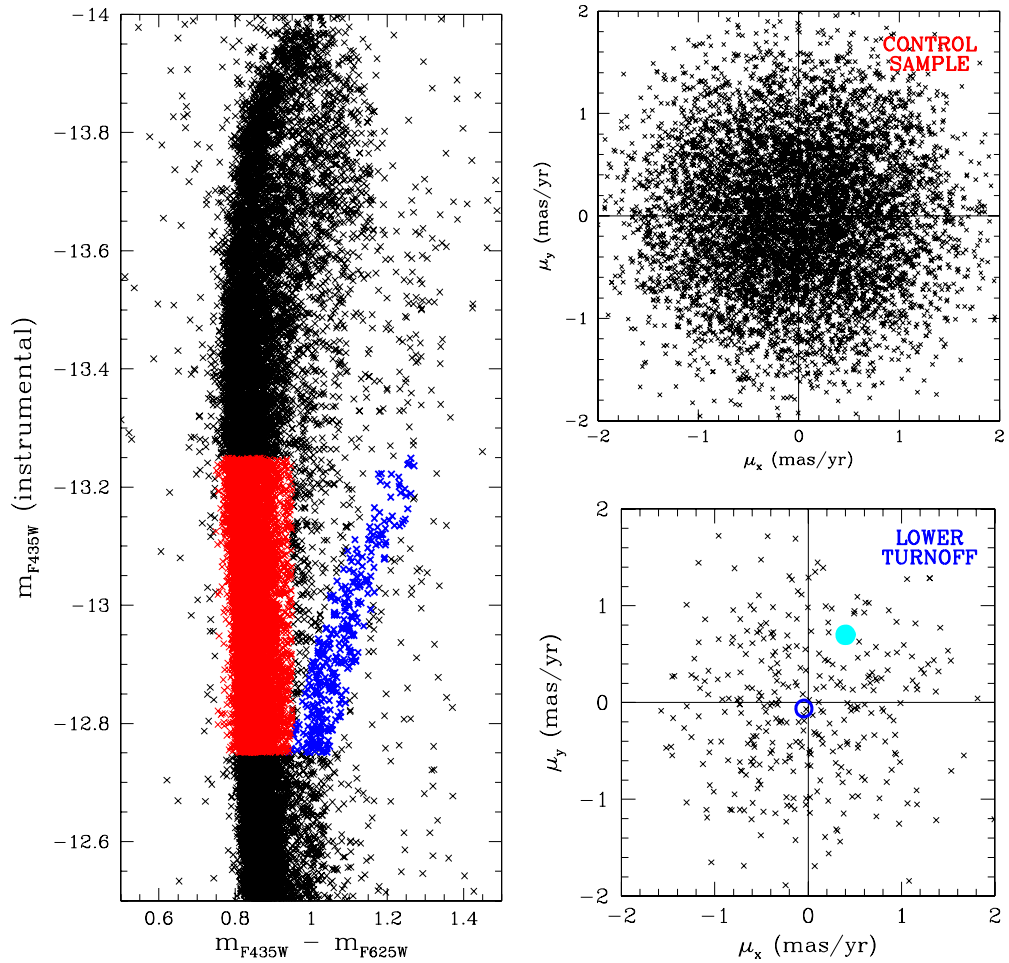

Figure 26. Left: color–magnitude diagram identifying the lower-turnoff population (blue in the online version) and the control population (red), which should have similar proper-motion errors. Lower right: the vector-point diagram for the control sample. Upper right: the vector-point diagram for the LTO population. The circle represents the 90% confidence region for our fit to the center of the distribution. The filled dot (cyan) shows the motion as measured by Ferraro et al. (2002).

(A color version of this figure is available in the online journal.)

the metal-rich population is moving with the cluster. We focus here on the lower-turnoff (LTO) stars, the SGB analog of the RGB-a stars.

The left panel of Figure 26 shows a close-up of the turnoff region for the stars for which we have good proper motions. We highlight the LTO population in blue, and a control sample

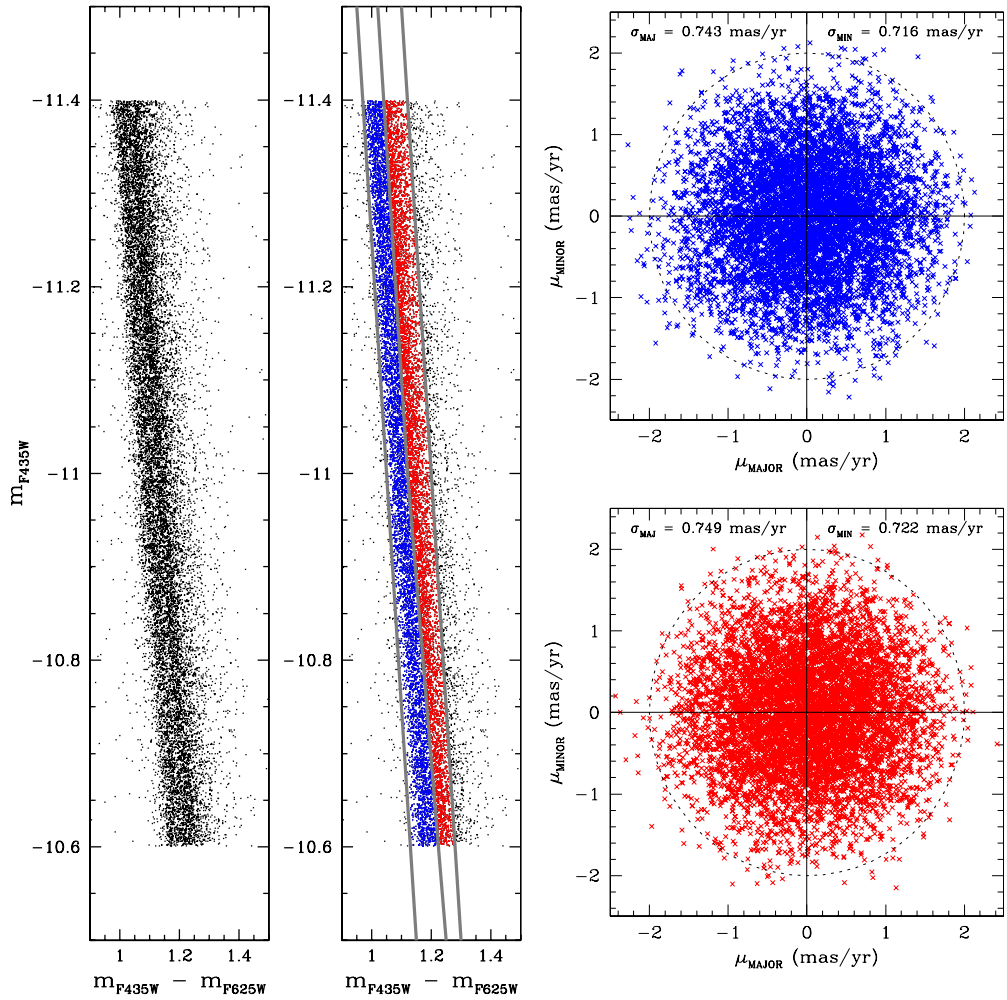

Figure 27. Dispersion for the main-sequence stars the central field. Left: CMD before selection. Middle: CMD with selected bMS and rMS highlighted. Upper right: PM distribution of the bMS stars, with the dispersions indicated at the top of the plot. Lower right: same for the rMS stars. Dashed circles are drawn for reference. The error in each dispersion is about 0.006 mas yr^{-1}.

(A color version of this figure is available in the online journal.)

with similar flux in $B_{\rm F435W}$ (and thus similar astrometric errors) in green. On the right, we show the proper motions for the two samples. It is clear that both distributions are centered on zero, meaning that they both share the bulk motion of the cluster. The cyan dot in the upper right panel shows the motion determined by Ferraro et al. (2002). The center of the μ_x distribution for the LTO population is -0.046 ± 0.040 mas yr^{-1}, and the μ_y center is -0.062 ± 0.040 mas yr^{-1}. Both are consistent with zero, and similarly consistent with the motion for the control population. We therefore conclude that all of the populations in the CMD are moving with the cluster and are phase-mixed. We note that the dispersions of the two populations are also the same, to within measurement errors (3%).

7.3. Motions for the Different MS Populations

Omega Cen was the first of the traditional GCs found to have multiple populations. The spread in metallicity along the giant branch has been known for many decades (Dickens & Woolley 1967; Freeman & Rodgers 1975), but only recently have we been able to trace the multiple populations down to the unevolved stars. Anderson (2002) found and Bedin et al. (2004) confirmed that the MS clearly bifurcates into a red and blue branch below $V \sim 20$. Unexpectedly, they found that the fractions of stars in the two populations are opposite to what one would expect based on the RGB populations and standard enrichment scenarios, which would have the bluer main-sequence population (bMS) being more metal poor (and more populous) than the redder main-sequence population (the rMS). Norris (2004) pointed out that this could be explained by assuming that the metal-richer population was super-enriched in helium. Villanova et al. (2007) then measured metallicities for stars in the two populations and found that the bluer stars were indeed more metal rich than the redder stars, in line with the helium explanation.

Since these initial discoveries of the split MS populations, the spatial distribution of the stars has been studied by Sollima et al. (2007) and by Bellini et al. (2009b). They find that the intermediate-metallicity population is more concentrated than the metal-poor population, both when the populations are identified on the RGB and on the MS. Kinematically, it was initially believed that the M-Int population did not share in the cluster rotation (Norris et al. 1997), but recent spectroscopy by Pancino et al. (2007) mentioned above finds that all three populations appear to share the same rotation, to within the 2 km s^{-1} measurement errors.

The radial velocities in the studies cited above come from all over the cluster, so they are able to probe the motions of stars with a global perspective. Here, we have proper motions in only two fields, one at the cluster center and one at about a 1.5 core

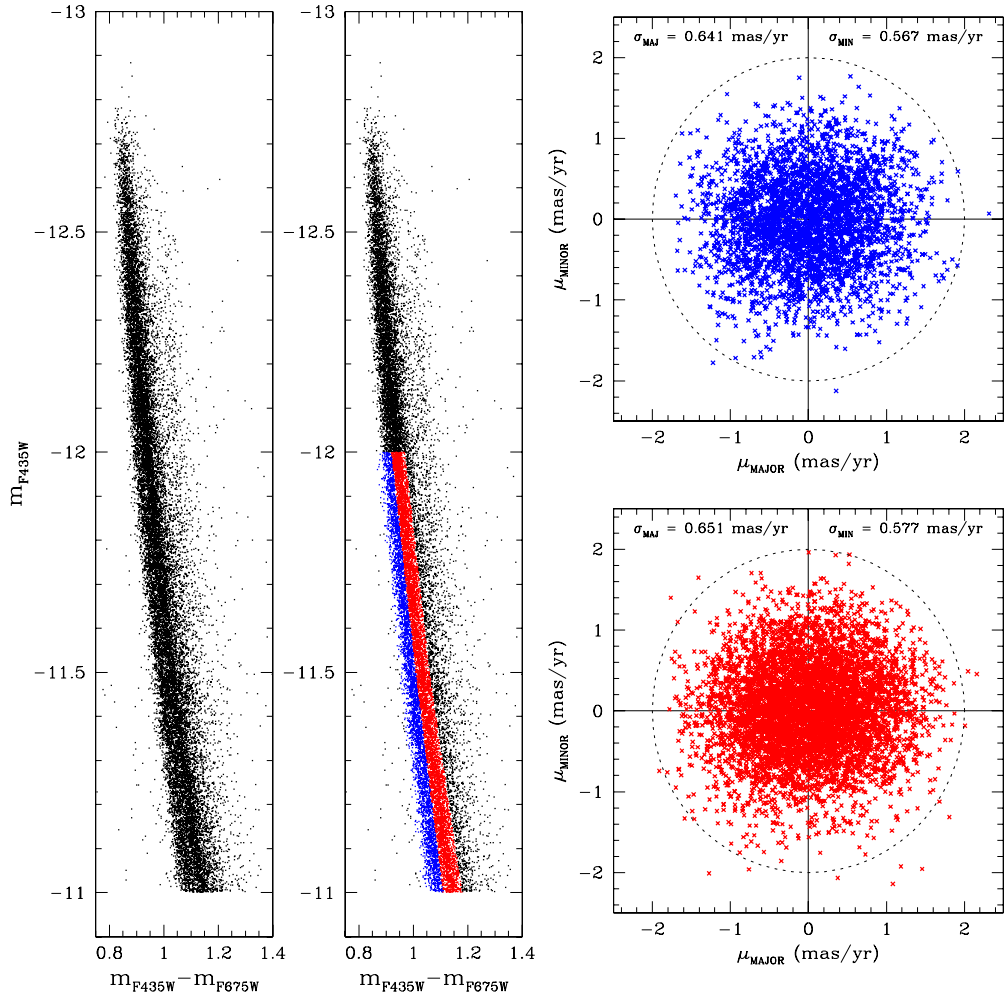

Figure 28. Same as Figure 27, but for the adjacent field. The error in each listed dispersion is ∼0.007 mas yr^{-1}.
(A color version of this figure is available in the online journal.)

radius out, along the major axis. Furthermore, we have motions only for stars on or below the SGB, so it is not possible to directly compare our motions against the radial velocities. Nevertheless, we can still compare the motions of the populations we have access to. In Figures 27 and 28, we compare the proper motions of the bMS and rMS stars in the central field and the major-axis field, respectively.

Figure 27 shows motions for the bMS and rMS stars in the central field. The left panel shows the CMD in the location where the two MS populations are clearly distinguishable in the central field, between an instrumental F435W magnitude of −11.4 and −10.6 (S/N ∼ 250). The middle panel shows our selection of the bMS and rMS stars. Finally, on the right, we show the vector-point diagrams with the motions for the two populations. We analyzed the two distributions to determine the (error-corrected) dispersions as marked at the top of each plot. The dispersions for the two populations in both the major- and minor-axes directions are the same to within the measurement errors (0.006 mas yr^{-1}). For both MS populations, the major-axis dispersion is about 3% greater than the minor-axis dispersion. All of the distributions have no mean motion, to within the measurement errors.

Figure 28 shows a similar plot for the adjacent field, which is centered at a radius of about 4′ (∼1.5r_c) along the SE major axis (see Figure 1). Again, we identified the bMS and rMS stars at a brightness along the MS where we could clearly distinguish them and, at the same time where we had good proper motions. The third column of panels shows the vector-point diagrams for the two populations. Again, the error-corrected dispersions noted at the top show no statistically significant differences between the populations.

The dispersion on the major axis is larger than that on the minor axis. This is what might naively have been expected from the fact that the dispersion provides the pressure that supports the shape of the system (rotation may generally contribute pressure as well, but we show in Section 5.2.3 of Paper II this is negligible near the center of the cluster). However, detailed axisymmetric anisotropic modeling would be required to fully interpret the differences between major-axis and minor-axis motion.

It bears repeating that any mean motion was removed from the proper motions during the data reduction stages, as discussed in Section 3.6.4. Hence, the motions as we have measured them here are unable to measure rotation directly. For that, one would need reference objects to measure against (e.g., Anderson & King 2003 measured the rotation of 47 Tuc in the plane of the sky using the background SMC stars). However, if there are multiple populations within the cluster and one population happens to be rotating relative to another, then we would expect this relative rotation to manifest itself as a bulk motion between the two populations. This would be most prominent in the major-axis field, because rotation in stellar systems typically decreases toward the center. Of course there would be no rotation in the plane of the sky if the cluster were edge-on, but van de Ven

et al. (2006) found the inclination of Omega Cen to be 48°. Therefore, we would expect some difference in observed bulk motion if different populations had different rotations.

Our analysis shows that the centers of the bMS and rMS distributions are the same in the major-axis direction, but differ by 3σ (0.037 mas yr^{-1} or 0.8 km s^{-1}, assuming a distance of 4.8 kpc) in the minor-axis direction. This is consistent with the possibility that the populations are rotating relative to each other, but the statistical significance of the result is only marginal (especially when taking into account the possibility of small residual systematic effects at levels below 1 km s^{-1}). We similarly examined the LTO of population in the major-axis field and found that it shows no systematic motion relative to the other populations. These findings are in agreement with the recent radial-velocity study by Pancino et al. (2007), who found that all the stars have the same rotational properties to within 2 km s^{-1}.

The motions we have measured here provide only an incomplete picture into the dynamical state of the cluster. Ideally, we would like to have both accurate proper motions and radial velocities, as well as population-identification information, for a large number of stars distributed throughout the cluster. This would allow us to distinguish what kinds of orbits are populated by the different stellar populations, giving us much more information than simple studies of spatial distributions, dispersions, or rotational components. To this end, we could augment our proper-motion catalog with motions for the brighter stars using the shorter exposures; there exist measured radial velocities for many of these stars and we would then have five of the six phase-space coordinates (lacking only the line-of-sight location). However, the size of the central field would still be a significant limitation to our ability to infer the global properties of the cluster.

8. CONCLUSIONS

We have performed a careful reduction of the large GO-9442 data set which mosaic-imaged the inner $10' \times 10'$ of Omega Cen with well-dithered *HST*/ACS observations. We constructed a 1.2 million star photometric catalog of positions and $B_{\rm F435W}$ and $R_{\rm F625W}$ magnitudes from these data, along with a 14,000 × 14,000 pixel stacked image of the field in the same reference frame as the catalog. We also reduced the data from two other ACS/WFC programs that overlap with the GO-9442 mosaic, but which covered only a single pointing (with medium-sized dithers). GO-10775 observed a central field and GO-10252 an adjacent field to the SE, roughly along the major axis. Accurate astrometric analysis of the data allowed us to determine proper motions for stars in these fields. The resulting proper-motion catalogs, with cuts applied to retain only the "high-quality" measurements, contain 53,382 stars in the central field and 19,593 stars in the major-axis field. The data products from our study are made publicly available as part of this paper (see Section 3.7).

We analyzed the positions of the observed stars to determine the cluster center. For this we used two separate methods, one based on isodensity-contour fitting, and one based on the so-called pie-slice method. In the latter method, we took particular care to model the effects of incompleteness, and to correct for them. The cluster centers thus determined each have an error bar of $\sim 1''$, and they agree to within the errors. Upon use of stars in common with the 2MASS catalog to calibrate to absolute coordinates, we find the center to be at $(\alpha, \delta) = (13{:}26{:}47.24, -47{:}28{:}46.45)$. We also used our proper-motion catalog to determine the kinematical center of the cluster, defined as the symmetry point of the proper-motion dispersion field on the projected plane of the sky. This represents the first time that the kinematic center of a GC has been accurately determined. Again, we used methods based on contours and pie slices, with consistent results. The kinematical center agrees with the star-count center to within its $\sim 2''$ uncertainties. And finally, we also determined the center of unresolved light in 2MASS data, again yielding a consistent result at the $\sim 2''$ level.

We computed the surface number-density profile of the cluster around its (newly determined) center. AS tests were used to correct for the effects of photometric incompleteness. Density profiles were determined for various ranges of stellar magnitude, but were generally found to be similar, independent of magnitude. A single-mass King model provides a reasonable fit to the inferred profiles. There is no evidence for a strong number-density cusp toward the center; in fact the density in the centermost bins appears smaller (at marginal significance) than that at somewhat larger radii ($R \approx 10''$).

The proper-motion dispersion increases gently inward from the core radius ($\sim$2.5 arcmin) to about $30''$, but flattens out at smaller radii. Detailed analysis in the central $15''$ shows little variation in kinematics with position. The dispersion does not increase appreciably toward the center, and the wings of the proper-motion distribution do not become more extended toward the center. There are no high-velocity outlier stars near the center that might be indicative of motion around an IMBH.

We examined the variation of velocity dispersion with mass along the MS and found that although the dispersion does increase for the lighter stars, the cluster is not yet in equipartition. This is in agreement with the findings in Anderson (2002), who found that the cluster does not exhibit the mass segregation that would be expected for a multi-mass King model in equipartition. These results are not surprising, given the long half-mass relaxation time of $\sim 10^{9.96\pm0.03}$ yr (McLaughlin & van der Marel 2005).

Omega Cen has long been known to have multiple stellar populations. The proper-motion catalog we have constructed here has enabled us to look for variations in kinematics between populations. The blue (bMS) and red (rMS) main sequence stars have very similar dynamical properties. This holds for both the central field and the adjacent field along the major axis, and is true both in terms of dispersion and mean rotation (the latter is not a trivial result, because Omega Cen is not believed to be edge-on; van de Ven et al. 2006). The similarity in rotational properties contrasts with the findings of Norris et al. (1997) based on radial velocities. However, it agrees with a more recent study by Pancino et al. (2007). The mean motion of the metal-rich turnoff population is consistent with that of the rest of the cluster. This is what would be expected for a (quasi-)equilibrium configuration, and disagrees with an earlier finding of Ferraro et al. (2002).

NGB08 argued for the presence of an IMBH in the center of Omega Cen based on a combination of two arguments. First, they measured the integrated line-of-sight velocity dispersion of unresolved light in two $5'' \times 5''$ fields, one believed to be on the cluster center and one at $R = 14''$ from the center. The dispersion in the central field (23.0 ± 2.0 km s^{-1}) exceeded that in the off-center field (18.6 ± 1.6 km s^{-1}), consistent with the presence of an IMBH of mass $4.0^{+0.75}_{-1.0} \times 10^4\ M_\odot$. Second, they measured the surface-brightness profile of unresolved light. They found it to have a shallow central cusp of logarithmic slope $\gamma = 0.08 \pm 0.03$, consistent with theoretical predictions for the

cusp induced by an IMBH (Baumgardt et al. 2005). The results from our new study have allowed us to test these arguments.

We determined the one-dimensional proper-motion dispersion of the stars in our catalog in each of the two fields studied by NGB08. For a canonical Omega Cen distance $D = 4.8$ kpc (van de Ven et al. 2006), the results translate to 18.9 ± 1.3 km s^{-1} and 19.0 ± 1.6 km s^{-1}, for the central and off-center fields, respectively. So we find no kinematical difference between the fields, and we also do not detect kinematical gradients elsewhere in the central $\sim 15''$. Moreover, we find that NGB08 did not actually observe the cluster center in their integral-field spectroscopy. The cluster center identified by NGB08 is $12''$ from our newly determined center. We demonstrate that this (and similar offsets in other previous determinations) is likely due to biases induced by overweighting of the small number of bright giants, or the limited region over which stars were measured (the central ACS chip in the case of NGB08, which covers only half the core). Here, we have included the more plentiful MS stars and we have measured them out to beyond one core radius. This yields a precise and unbiased handle on the center of the cluster density distribution, as confirmed by our independent center determination from *HST* proper motion and 2MASS unresolved light data.

The existence of a density cusp in Omega Cen, as reported by NGB08, has also not been confirmed by our analysis. Since they calculated their density profile around an incorrect estimate of the center, it is unclear what physical meaning their result may have. Either way, we showed here that use of unresolved integrated light, as was done by NGB08, is not the best way to constrain the cluster density profile. This method does not primarily measure the flux from a large number of unresolved stars, but instead is sensitive to the large-radii scattered PSF wings of bright giants. This method therefore suffers more from shot noise (biases related to small-number statistics) than a measurement of the number-density profile. This is particularly important in a (nearly) homogeneous core such as that in Omega Cen, since shot noise will always cause some areas of high apparent density to exist by chance. The error bars on our number-density profile around the NGB08 center are such that the apparent density enhancement there is consistent with being a statistical fluctuation. The number-density profile determined by us around the newly determined center also shows little evidence of a significant cusp toward the center, although a shallow cusp may not be ruled out.

In summary, our results do not validate the arguments put forward by NGB08 to suspect the presence of an IMBH in Omega Cen. However, this does not mean that such an IMBH may not be present after all. Our new proper-motion catalog far exceeds the quality and quantity of the kinematical data in the central arcmin previously available. This provides the opportunity to study the central dynamics of Omega Cen at a level of detail that is unmatched by almost all other clusters, with the possible exception of 47 Tuc (McLaughlin et al. 2006). In Paper II, we therefore present a new detailed study of the dynamics and density profile of Omega Cen, with the primary goal of exploiting the new data to constrain the mass of any possible IMBH.

J.A. acknowledges the support from STScI grant GO-10401. We are grateful to Ivan King and Mario Livio for feedback, advice and encouragement during the course of this project. Suggestions from the referees helped us improve the presentation of our results.

REFERENCES

Anderson, J. 2002, in ASP Conf. Ser. 265, ω Centauri: A Unique Window into Astrophysics, ed. F. van Leeuwen, J. Hughes, & G. Piotto (San Francisco, CA: ASP), 87
Anderson, J. 2005, in The 2005 HST Calibration Workshop, ed. A. M. Koekemoer, P. Goudfrooij, & L. Dressel (Baltimore, MD: STScI)
Anderson, J., & King, I. R. 2003, AJ, 126, 772
Anderson, J., & King, I. R. 2006, ACS/ISR 2006-01, PSFs, Photometry, and Astrometry for the ACS/WFC (Baltimore, MD: STScI)
Anderson, J., et al. 2008, AJ, 135, 2055 (A08)
Baumgardt, H., Hut, P., Makino, J., McMillan, S., & Portegies-Zwart, S. 2003a, ApJ, 582, L21
Baumgardt, H., Makino, J., & Hut, P. 2005, ApJ, 620, 238
Baumgardt, H., Makino, J., Hut, P., McMillan, S., & Portegies-Zwart, S. 2003b, ApJ, 589, L25
Bedin, L. R., Piotto, G., Anderson, J., Cassisi, S., King, I. R., Momany, Y., & Carraro, G. 2004, ApJ, 605, L125
Bellini, A., Piotto, G., Bedin, L. R., Anderson, J., Platais, I., Momany, Y., Moretti, A. P., & Ortolani, S. 2009a, A&A, 493, 959
Bellini, A., Piotto, G., Bedin, L. R., King, I. R., Anderson, J., Milone, A. P., & Momany, Y. 2009b, A&A, 507, 1393
Castellani, V., et al. 2007, ApJ, 663, 1021
Dickens, R. J., & Woolley, R. v. d. R. 1967, R. Obs. Bull., 128, 255
Drukier, G. A., & Bailyn, C. D. 2003, ApJ, 597, L125
Ferraro, F. R., Bellazzini, M., & Pancino, E. 2002, ApJ, 573, L95
Ferraro, F. R., Sollima, A., Pancino, E., Bellazzini, M., Straniero, O., Origlia, L., & Cool, A. M. 2004, ApJ, 603, L81
Freeman, K. C., & Rodgers, A. W. 1975, ApJ, 201, L71
Fruchter, A. S., & Hook, R. N. 2002, PASP, 114, 144
Gebhardt, K., Rich, R. M., & Ho, L. C. 2002, ApJ, 578, L41
Gebhardt, K., Rich, R. M., & Ho, L. C. 2005, ApJ, 634, 1093
Genzel, R., et al. 2003, ApJ, 594, 812
Gerssen, J., van der Marel, R. P., Gebhardt, K., Guhathakurta, P., Peterson, R., & Pryor, C. 2002, AJ, 124, 3270 (addendum: 2003, AJ, 125, 376)
Ghez, A. M., et al. 2005, ApJ, 620, 744
Harris, W. E. 1996, AJ, 112, 1487
Koekemoer, A. M., McLean, B., McMaster, M., & Jenker, H. 2005, in The 2005 HST Calibration Workshop, ed. A. M. Koekemoer, P. Goudfrooij, & L. L. Dressel (Baltimore, MD: STScI), 417
Kong, A. K. H. 2007, ApJ, 661, 875
Leonard, P. J. T., & Merritt, D. 1989, ApJ, 339, 195
McLaughlin, D. E., Anderson, J., Meylan, G., Gebhardt, K., Pryor, C., Minniti, D., & Phinney, S. 2006, ApJS, 166, 249
McLaughlin, D. E., & van der Marel, R. P. 2005, ApJS, 161, 304
McNamara, B. J., Harrison, T. E., & Anderson, J. 2003, ApJ, 595, 187
Norris, J. E. 2004, ApJ, 612, L25
Norris, J. E., Freeman, K. C., Mayor, M., & Seitzer, P. 1997, ApJ, 487, L187
Noyola, E., & Gebhardt, K. 2006, AJ, 132, 447
Noyola, E., Gebhardt, K., & Bergmann, M. 2008, ApJ, 676, 1008 (NGB08)
Pancino, E., Ferraro, F. R., Bellazzini, M., Piotto, G., & Zoccali, M. 2000, ApJ, 534, L83
Pancino, E., Galfo, A., Ferraro, F. R., & Bellazzini, M. 2007, ApJ, 661, L155
Pietrinferni, A., Cassisi, S., Salaris, M., & Castelli, F. 2006, ApJ, 642, 797
Platais, I., Wyse, R. G., Hebb, L., Lee, Y.-W., & Rey, S.-C. 2003, ApJ, 591, L127
Pooley, D., & Rappaport, S. 2006, ApJ, 644, L45
Portegies Zwart, S. F., & McMillan, S. L. W. 2002, ApJ, 576, 899
Sirianni, M., et al. 2005, PASP, 117, 1049
Skrutskie, M. F., et al. 2006, AJ, 131, 1163
Sollima, A., Ferraro, F. R., Bellazzini, M., Origlia, L., Straniero, O., & Pancino, E. 2007, ApJ, 654, 915
Ulvestad, J. S., Greene, J. E., & Ho, L. C. 2007, ApJ, 661, L151
van de Ven, G., van den Bosch, R. C. E., Verolme, E. K., & de Zeeuw, P. T. 2006, A&A, 445, 513
van den Bosch, R., de Zeeuw, T., Gebhardt, K., Noyola, E., & van de Ven, G. 2006, ApJ, 641, 852
van der Marel, R. P. 2004, in Coevolution of Black Holes and Galaxies, ed. L. C. Ho (Cambridge: Cambridge Univ. Press), 37
van der Marel, R. P., & Anderson, J. 2010, ApJ, 710, 1063 (Paper II)
van der Marel, R. P., Gerssen, J., Guhathakurta, P., Peterson, R. C., & Gebhardt, K. 2002, AJ, 124, 3255
van Leeuwen, F., Le Poole, R. S., Reijns, R. A., Freeman, K. C., & de Zeeuw, P. T. 2000, A&A, 360, 472
Villanova, S., et al. 2007, ApJ, 663, 296